ASTROBIOLOGY
Volume 21, Number 4, 2021

DOI: 10.1089/ast.2019.2164

Research Article

Acid Mine Drainage as Energizing Microbial Niches for the Formation of Iron Stromatolites: The Tintillo River in Southwest Spain

Elizabeth Chacon-Baca,[1] Ana Santos,[2,3] Aguasanta Miguel Sarmiento,[4,5] Ana Teresa Luís,[4,6] Maria Santisteban,[4,5] Juan Carlos Fortes,[4,5] José Miguel Dávila,[4,5] Jesus M. Diaz-Curiel,[7] and Jose Antonio Grande[4,5]

Abstract

The Iberian Pyrite Belt in southwest Spain hosts some of the largest and diverse extreme acidic environments with textural variation across rapidly changing biogeochemical gradients at multiple scales. After almost three decades of studies, mostly focused on molecular evolution and metagenomics, there is an increasing awareness of the multidisciplinary potential of these types of settings, especially for astrobiology. Since modern automatized exploration on extraterrestrial surfaces is essentially based on the morphological recognition of biosignatures, a macroscopic characterization of such sedimentary extreme environments and how they look is crucial to identify life properties, but it is a perspective that most molecular approaches frequently miss. Although acid mine drainage (AMD) systems are toxic and contaminated, they offer at the same time the bioengineering tools for natural remediation strategies. This work presents a biosedimentological characterization of the clastic iron stromatolites in the Tintillo river. They occur as laminated terraced iron formations that are the most distinctive sedimentary facies at the Tintillo river, which is polluted by AMD. Iron stromatolites originate from fluvial abiotic factors that interact with biological zonation. The authigenic precipitation of schwertmannite and jarosite results from microbial–mineral interactions between mineral and organic matrices. The Tintillo iron stromatolites are composed of bacterial filaments and diatoms as *Nitzschia aurariae*, *Pinnularia aljustrelica*, *Stauroneis kriegeri*, and *Fragilaria* sp. Furthermore, the active biosorption and bioleaching of sulfur are suggested by the black and white coloration of microbial filaments inside stromatolites. AMD systems are hazardous due to physical, chemical, and biological agents, but they also provide biogeochemical sources with which to infer past geochemical conditions on Earth and inform exploration efforts on extraterrestrial surfaces in the future. Key Words: Mineralization—Microbe–mineral interactions—Biosignatures—Geomicrobiology—Mars—Extremophiles—Acidophiles—Extreme environments. Astrobiology 21, xxx–xxx.

1. Introduction

Throughout Earth's history, mineral-microbial interactions have resulted in a wide variety of macroscopic organic sediments. Stromatolites, distinguished by their alternate lamination, stand out as the oldest and most conspicuous evidences in the fossil record of life (Buick *et al.*, 1981; Grotzinger and Knoll, 1999; Westall, 2005). The alternate lamination of stromatolites can preserve the interplay between periodic sediment supply and biological changes in mat communities, including pauses in the sedimentation rate (Golubic *et al.*, 2000). Although the vast majority of modern and fossil stromatolites are composed of calcium carbonate, fossil stromatolites of siliceous, phosphate, iron, manganese,

[1]Departamento de Geología, Facultad de Ciencias de la Tierra, Universidad Autónoma de Nuevo Léon (UANL), Linares, México.
[2]Department of Applied Geosciences, CCTH—Science and Technology Research Centre, University of Huelva, Huelva, Spain.
[3]Applied Geosciences Research Group (RNM276), Departamento de Ciencias de la Tierra, Facultad de Ciencias Experimentales, Universidad de Huelva, Huelva, Spain.
[4]Department of Water, Mining and Environment, Scientific and Technological Center of Huelva, University of Huelva, Huelva, Spain.
[5]Sustainable Mining Engineering Research Group, Department of Mining, Mechanic, Energetic and Construction Engineering, Higher Technical School of Engineering, University of Huelva, Huelva, Spain.
[6]GeoBioTec Research Unit, Department of Geosciences, University of Aveiro, Aveiro, Portugal.
[7]Departamento de Geología, Escuela Técnica Superior de Ingenieros de Minas, Madrid, Spain.

and sulfate also occur, either as primary precipitates or, more commonly, as diagenetic replacement (Chauhan, 1979; Lundberg and McFarlane, 2011; Riding, 1999; Riding, 2011; Lozano and Rossi, 2012; Sallstedt *et al.*, 2018). Today, iron stromatolites are formed in unique modern settings with complex biogeochemical interactions that serve as geochemical, mineral, biological, and environmental sources. The early record of life suggests that iron metabolism was not only ubiquitous, but it was also among the most ancestral biochemistries. For instance, the distribution of iron-oxidizing bacteria that are capable of switching from chemolithoautotrophy to photoautotrophy in deep-sea hydrothermal settings (Ishii *et al.*, 2015) also indicates that dissimilatory Fe(II) oxidation is probably an ancient energy metabolism (Ilbert and Bonnefoy, 2013).

Iron is not only the most abundant metal on Earth, but also about 90% of all iron formations are derived from Precambrian banded iron formations (BIFs) (Pilchin and Eppelbaum, 2009). However, pyrite (FeS_2) is the most abundant iron–sulfur mineral at Earths' surface, and it is present in igneous, metamorphic, and sedimentary rocks (Rickard and Luther, 2007). Because iron and sulfur were abundant and accessible, early life was probably fueled by multiple oxidation and reduction reactions (Knoll, 2003; Canfield *et al.*, 2006; Planavsky *et al.*, 2009; Lalonde and Konhauser, 2015).

Current polluted environments known as acid mine drainage (AMD) contain copious amounts of iron and sulfur, and therefore, they are excellent modern analogues of ancient scenarios. AMD settings, which are rich in Fe^{2+} ions, trace elements such as arsenic (As), and other heavy metals, represent the contaminated tailings of the mining industry. The oxidation of sulfide minerals (as pyrite) in AMD causes high acidity and high concentrations of soluble metals (Konhauser, 2007). Despite their toxicity with regard to health, environment, soil, and water resources, AMD fosters complex biogeochemical interactions that maintain a rich geomicrobiological diversity pool.

Recent trends in mineral–microbial interactions have led to the proliferation of studies in AMD as niches for microbial colonization (Bird *et al.*, 2011; Caraballo *et al.*, 2011; Nordstrom *et al.*, 2015; Huang *et al.*, 2016; Shuster *et al.*, 2018; Gavrilov *et al.*, 2019; Hasiotis and Brake, 2019; Lukhele *et al.*, 2020; Rivera *et al.*, 2019; Gao *et al.*, 2020). Such extreme environments are also settings that sustain the formation of recent iron stromatolites that accrete as iron terraces. As documented by pioneer studies, the AMD in the Tintillo river is one of the few places worldwide where extensive terraced iron formations readily form (Sánchez-España *et al*. 2005b, 2006, 2007). Throughout this article, the term ''TIFs'' will be used to refer to terraced iron formations as used by Sánchez-España *et al.* (2007). We define terracettes as depositional facies that have a geomorphological attribute of narrow, short, and rarely parallel treads at a steeper angle than other depositional morphologies (Anderson, 1972). These features generally form in carbonate travertine systems. Although Fe-rich sediments are globally distributed, their occurrence as TIFs is rather scarce (Table 1).

Stromatolites grow and accrete by trapping, binding, and precipitation of sedimentary particles by benthic microbial communities (Awramik, 1977). Yet, one of the greatest challenges in stromatolitic lamination is the distinction between biotic and abiotic processes, which are by far more complex in iron stromatolites (Brake *et al.*, 2001, 2004, 2014). Previous studies at Tintillo suggest that iron stromatolites result from the alternation between abiotic factors (hydrological process) and biological factors where iron precipitation is mediated by bacterial metabolism (Sánchez-España *et al.*, 2007). Studies have also shown that TIFs are mainly influenced by cyclic seasonal variations: cooler temperatures in winter correlate with higher flow conditions that increase pH and favor mineral precipitation. Concordantly, higher temperatures correlate with lower streamflow, iron precipitation, and higher bacterial populations.

What is less clear is the relation between photosynthetic eukaryotes and the mineral matrix, especially in the dry season. In the present study, our goal was to analyze the occurrence of photosynthetic eukaryotes in Tintillo TIFs in seasons when accretion is at minimum. Since TIFs display multiple scalar variations, a second goal for this study was to assess their astrobiological relevance from a morphological perspective. To characterize TIFs at the geochemical, mineral, and biological level, we employed a combination of qualitative and quantitative approaches.

Gradients generated by concurrent biogeochemical processes often develop into multiple-scale biosignatures. This study was designed to contribute to this growing research area by revising a morphological first approach in astrobiology. As long as modern space exploration depends on large-scale morphological recognition, AMD systems have the potential to provide good models with which to study the occurrence of structures, processes, and patterns.

2. Geological Setting

The Iberian Pyrite Belt (IPB) in southwest (SW) Spain contains unusual AMD deposits that have been studied over the course of decades. This area forms part of the IPB and the volcano-sedimentary complex, which are dominated by volcanic-siliceous rocks (rhyolitic todacitic tuffs, breccias and lava flows, tuffites) and graywackes and shales, where no carbonate or alkaline materials are present (Sánchez-España *et al*., 2005a, 2006). The area under study here corresponds to the Tintillo deposit, which is polluted by AMD and $\sim$10 km long, 40 m wide, covering an area of 57 km^2. This stream is characterized by receiving exclusively the input of acid sulfate waters from the four main springs that emanate from the base of sulfide-bearing waste-rock piles. The larger spring is from a vast open-pit ($\sim$1 km long and 40 m deep) that is situated in the surroundings of Corta Atalaya. The three other fluvial inputs are from the Barrizal, Gangosa, and Escorial tributary creeks of the Tintillo river (Sánchez-España *et al*., 2005b).

The present study was conducted in the Tintillo river contaminated by the Río Tinto area, located to the North of Huelva, a province of SW Spain (37°43′0″N; 6°38′37″O). The area under study is located 7.3 km north of Campillo (Fig. 1). The mean annual temperature is 16.1°C, with a mean minimum temperature of 9°C (between December and January) and a mean maximum temperature of 24°C (July and August), reaching maximum values of 35°C in these 2 months. The climate zone corresponds to Continental Mediterranean, with a mean annual precipitation of 849.1 mm and a mean minimum precipitation around 3.65 mm between

Table 1. Iron Stromatolites in Reported Acid Mine Drainage Sites with Terraced Iron Formations

Locality	*pH/Temperature (°C)*	*Facies*	*Mineralogy*	*References*
Carnoulès creek, SE flank of the Massif Central, France	2.8/15°C	Fe-As-rich accretions; ridged-pool TIFs (15–20 cm thick)	Amorphous $Fe(OH)_3$ or $Fe(SO_4)_3$; Fe^{3+} arsenate crystals	Leblanc *et al.* (1996); Bruneel *et al.* (2006)
Angel Terrace in the Mammoth Hot Springs	7.4–8.6/53–88°C	Pond facies, proximal slope	Aragonite	Fouke *et al.* (2000); Konhauser (2007)
Alto de la Mesa, Río Tinto, Spain	2.3/0–40°C	Biofilms; 25 cm depth	Hematite, goethite, jarosite	Fernández-Remolar *et al.* (2003); Amils *et al.* (2007); Loiselle *et al.* (2018)
Green Valley coal mining site (GVS), Indiana	3/n.d.	TIFF pools, Fe-rich biofilms, AMD channel bottom	Amorphous iron hydroxides, Al-hydroxides	Brake *et al.* (2004); Sheng *et al.* (2016); Hasiotis and Brake (2019)
Tintillo, Huelva, Spain	2.6/25.2°C	Point bar, height = 50 cm	Schwermanite, goethite, jarosite	Sánchez-España *et al.* (2007)
San Telmo, San Miguel, and Tharsis mines, Huelva, Spain	3.34–3.41/ 13.9–26.5°C	Gossans riverine TIFs	Goethite and hematite, argentojarosite, hydroniumjarosite, gypsum, Qz	Sarmiento (2007); Sánchez-España *et al.* (2008)
Chocolate pots hot springs, YNP, United States	5.4–7.8/37–54°C	Channel phototrophics mats and TIFs	Ferrihydrite mats, siliceous ferrihydrite, goethite, hematite, and nontronite (diagenetic)	Parenteau and Cady (2010)
Lower Red Eyes AMD, Somerset County, PA	2.4–4.0/ 28.0–73.2°C	Iron mounds, terraces and pools, 5 height; 30 cm depth	Goethite, schwertmanitte	Brown *et al.* (2011); Burgos *et al.* (2012)
Joseph's Coat/Rainbow Springs, YNP, United States	2.4–3.6/n.d.	Fe-microbial mats	Jarosite, goethite, ferrihydrite, hematite, Fe-oxyhydroxides	Kozubal *et al.* (2012)
Santiago river, Cordillera Negra, Peru	3.4/n.d.	Moss microterraces at 3800 m (masl)	Schwertmannite, tooeleite, AL-Fe hydroxids	Sevink *et al.* (2015)
Iron Mountain Mine, CA	2.7–3.1	Pipe scale textures downstream	Schwertmannite, poorly crystalline goethite, jarosite, schwertmannite, goethite	Williams *et al.* (2017)
Appalachian bituminous coal basin (Mine No. 29 in Scalp Level, PA)	2.89/13.3°C	Natural and engineered TIFs (bioreactors); 2 cm thick surface sediments	Schwertmannite, jarosite	Sheng *et al.* (2017)
Mount Morgan mine, Queensland, Australia	3.2/n.d.	TIFs step-like bench facies	Schewertmannite, goethite, gypsum, jarosite, pyrite (FeS_2), pyrrhotite, chalcopyrite ($CuFeS_2$), sphalerite; schwertmannite/goethite	Shuster *et al.* (2018)
Inland sabkha mineralized, Sabkha Oum Dba, Morocco	7.89–8.13/ 16.6–22.8°C	Marginal cm-microterracettes and microbial mats	Evaporites (sulfates and carbonates) clay minerals, $CaCO_3$, Mg-calcite precipitates	Barbieri and Cavalazzi (2018)
Dalloi Volcano hot springs, Ethiopia	3/55°C	Sulfur terracettes and deposits, muddy evaporites	Iron-oxide crusts, clays, evaporites	Cavalazzi *et al.* (2019)
Pamukkale Geothermal Field (PGF), SW Turkey	6.4/28.8°C	Terrace mounds (pond/ terraced slope), Ca-SO_4 types	Ca-SO_4 type, Qz, aragonite	Alçiçek *et al.* (2018)
Iron travertines, Ilia, Italy	5.88–6.45/ 60.9–63.7°C	Botroydal travertines with a Fe- and Ca-rich cm-banding	Iron travertines, ferrihydrite, halitearagonite, calcite, Ca-rich orange laminae	Kanellopoulos *et al.* (2019)

AMD = acid mine drainage; masl = meters above sea level; TIF = terraced iron formation.

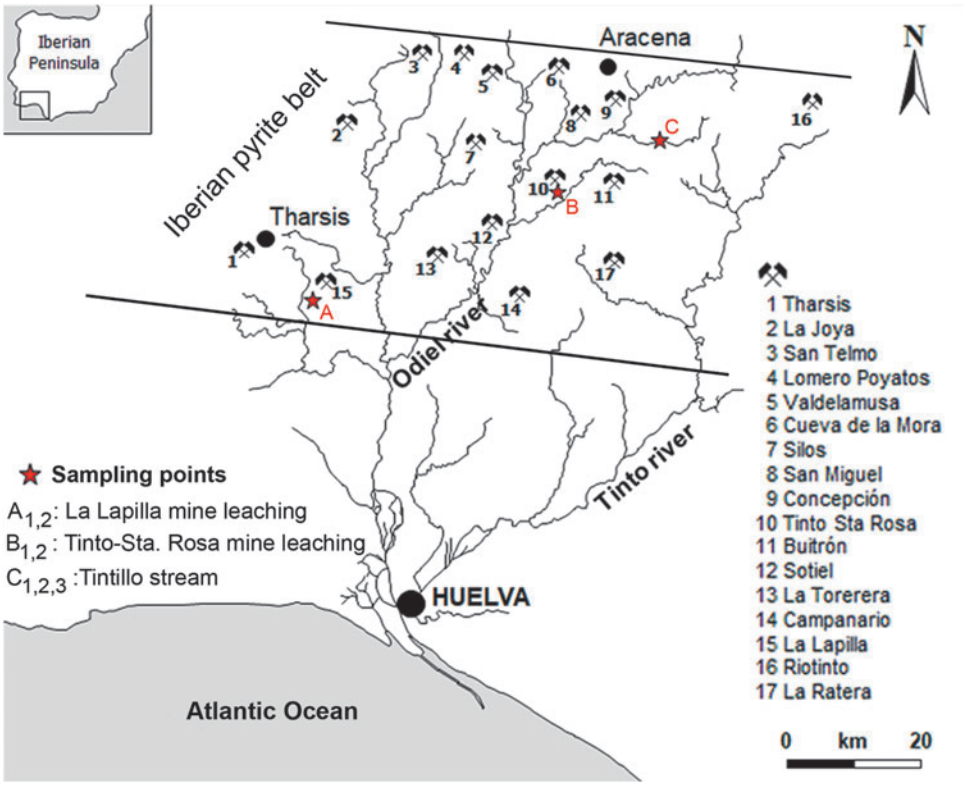

FIG. 1. Location map of the Tintillo AMD river in southern Spain. The hydrological map shows main localities with AMD tails, waste rock dams, and sampling points (red stars). AMD, acid mine drainage.

July and August (Tavira, 2016). Previous works have reported Fe-rich microbial laminated muds and emphasized the profuse development of microbial mats under the influence of biotic and abiotic factors (Sánchez-España *et al*., 2005b, 2006, 2007). Caraballo *et al.* (2011) documented the seasonal variations in the formation of Al- and Si-rich Fe stromatolites in the highly polluted AMD of Agua Agria Creek (Tharsis). These authors characterized the chemical and mineralogical composition of Fe stromatolites and confirmed the prominent role of diatoms in their formation.

The Tintillo is a meandering river with dendritic tributaries that runs on gently inclined floodplains and decreases in slope in the downcurrent direction. Tintillo stream waters run through shallow water subenvironments toward the distal parts of the system before it confluences with the Odiel river (Sánchez-España, 2007). The geomorphology in Tintillo AMD is dominated by gradational terraces that extend along the lateral stream of mine tailings (Sánchez-España *et al.*, 2005a, 2007). In this context, the sulfurous waters of Tintillo river, which are polluted by AMD, can be defined as an extreme habitat in terms of their very low mean pH (near 2.5) and high concentration of heavy metals, especially ferric iron, copper, zinc, and sulfate (López-Archilla and Amils, 1999; Aguilera *et al*., 2006). The Tintillo shores are characterized by the presence of extremophiles vegetation such as *Cistus ladanifer*, the endemic heath *Erica andevalensis*, *Pinus pinea*, and *Pinus pinaster* (Santa-Bárbara and Valdés, 2008).

3. Materials and Methods

This study included both field and laboratory analyses. Fieldwork consisted of geochemical measurements of surface waters, mapping, facies description, photo documentation, and sampling of solid TIFs. Based on the work of Sánchez-España *et al.* (2007), selected sampling points along the main course of the Tintillo river were visited during the summer of 2018 (Fig. 1). Samples taken from Tintillo surface waters were tagged as T. (V 2018). To evaluate the evolution of water geochemistry, this work included a comparison with other localities with the formation of TIFs in Tintillo Santa Rosa [T.S. (P 2003) and T.S. (V 2003)] sampled in spring and summer of 2003, respectively. Other included nearby sites without the presence of stromatolites were from La Lapilla stream, tagged as [L. (I 2003) and L. (P 2004)], taken in winter of 2003 and spring of 2004, respectively. We also included TIFs previously sampled in summer of 2004 T. (V 2004) and summer of 2015 T. (V 2015).

3.1. Fieldwork: measurements on site and sampling

Temperature (T), pH, redox potential (Eh), and electrical conductivity (EC, µS/cm or mS/cm, at 25°C) were recorded *in situ* with a multiparametric portable device (CrisonMM40) and a measuring scale of up to −2 pH units. The pH meter range was between 0.00 and 14.00 pH with a 0.01 pH resolution and a ±0.02 pH accuracy, and it was calibrated with WTW standard solutions (pH 2.00, 4.01, and 7.00); the redox potential was checked with Hanna standard

solutions (240 and 470 mV). For cations and metal analysis, two water samples were taken; to avoid metal precipitation, samples were acidified in the field to pH <2 with Suprapur HNO_3 (2%). Samples were kept in the dark at 4°C in 75 mL sterilized polyethylene bottles during the transport to the laboratory.

For sedimentological analysis, two fresh cross-sectional TIFs samples were collected from Tintillo river, tagged as P282 and P295 (in blocks of 50×20 cm), and kept cold at 4°C until immediate laboratory analysis. For comparison and as a negative control, ~100 g of sediment samples without (TIFs) was taken from the river bedrock. Algal biofilms attached to TIFS rims were sampled, fixed with a formaldehyde solution (4% v), and stored in a light-protected flask for further analysis.

3.2. Analytical methods

3.2.1. Water chemical analysis. The concentration of dissolved Al, As, Ca, Cr, Cu, Fe, Mg, Mn, Ni, Pb, Si, and Zn was determined by inductive coupling plasma atomic emission spectrometry (ICP-AES; Jobin-Ybon Ultima2). Calibrations were performed at the beginning and at the end of each analytical series by using a multielement standard solution prepared from certified standards supplied by SCP SCIENCE. The detection limits were calculated on average after three repeats, and the standard deviations of 10 blanks were also estimated. Certified Reference Material SRM-1640 NIST and interlaboratory standard IRMM-N3 wastewater test material were used according to the European Commission Institute for Reference Materials and Measurements. The detection limits for larger cations were: 200 μg/L for Al, Fe, Mn, Mg, Si; 500 μg/L for Ca; for trace elements, they were 50 μg/L for Zn, 5 μg/L for Cu, 2 μg/L for As, and 1 μg/L for the rest of the elements.

3.2.2. Sedimentology. A granulometry analysis was carried out to obtain in-depth information on TIF lamination. A subset of collected field samples of TIFs were air-dried at room temperature, ground, and sieved to <2 mm. TIF fractions and controls were processed by forcing the material through a 2-mm screen, by hand or with a large rubber stopper, and stored. Weight measurements were made and recorded on the 20- to 75-mm, 5- to 20-mm, and 2- to 5-mm fractions.

3.2.3. Petrography and compositional analysis of TIFs. Two petrographic-thin sections along the *x* and *z* axes were made, using a GTS polyester casting resin (Modulor GmbH), and analyzed by optical microscopy using a Nikon ECLIPSE TS100 inverted microscope coupled to a DS-Fi2 Camera with Digital Sight Unit DS-U3. To investigate whether lamination textures were correlated with chemical variations, dry TIF carbon-coated samples were examined under a JEOL JSM-5410 scanning electron microscope (SEM). For a quantitative compositional map of TIF samples, a fitted wavelength-dispersive spectrometer was used under the following conditions: accelerating voltage was 15 kV, the probe current was 20 nAmp, and beam diameter was 5 μm. Twelve TIF subsamples from P-281 (*x* axis) and P-281 (*z* axis) were analyzed, and 13 elements were determined (Si, Ca, Zn, Mg, Al, K, Cu, As, Cl, Fe, Pb, Mn, and S). One advantage with this analysis is that it avoided the problem of sample disruption, since TIFs are fragile and delicate. Several gold-coated TIF samples were studied under a SEM (JEOL JSM-5410) using an accelerating voltage of 15 kV and a beam current between 0.5 and 3 nAmp to observe the morphology and distribution of the constituent minerals.

3.2.4. Microbial analysis. TIF samples were analyzed under a NIKON Eclipse E200 microscope (Plan UW 20X) coupled to a DS-Fi2 Camera with Digital Sight Unit DS-U3. Also, some permanent slides, after gold coating, were analyzed under a SEM (JEOL JSM-5410) using an accelerating voltage of 15 kV and a beam current between 0.5 and 3 nAmp.

4. Results

4.1. Water geochemistry

The Tintillo water chemistries are presented in Table 2. Acid waters exhibit a pH that ranges between 2.6 and 2.9 in the selected sampling sites; the pH remains relatively constant along the stream course up to its confluence with the Odiel river (Fig. 1). Tintillo waters show a high oxidation potential (above 600 mV) and an electrochemical conductivity above 12 μS/cm. The variation in the As concentration is evident, with values ranging below the detection limit. Other measured elements show a high temporal stability, except for Si, whose lower concentration correlates with a decrease in As and Pb. The concentration of Fe and Ca is much lower in streams without stromatolites than in streams with stromatolites, with concentrations that do not exceed 20 mg/L of Fe and 57 mg/L of Ca (Table 2).

4.2. Depositional facies and TIFs

The Tintillo AMD river discharges acidified reddish waters along a main channel bordered by a deciduous shrub forest and red shales. The marginal zonation of shales caused by sulfur precipitates suggests seasonal precipitation (Fig. 2a, b). The geomorphology of Tintillo produced by transport, erosion, and depositional processes includes aqueous subenvironments and their associated sedimentary structures, which can be grouped into four depositional facies: (1) gossans and stream deposits, such as pebbles and boulders, from proximal to distal facies; (2) marginal channel facies characterized by benthic and planktonic microbial mats with minerals precipitated around shales; (3) point bars streams with iron terracettes or TIFs; and (4) small oxbow lakes and creeks. TIFs are the most conspicuous facies in Tintillo (Fig. 2c, d), and they form by erosion and inundation episodes by circulating AMD waters. They occur as downstream low-relief crenulated ridges with 0.3–0.5 m steep slopes (0.5–1 m in diameter), which confine polygonal red pools (Fig. 2e, f).

The polygonal geometry of pools breaks in those areas where channels are wider (more than 7 m across) and where sinuosity and turbulent flow are higher (Fig. 3a). Ridged TIFs exhibit a macroscale corrugated surface with intercalated layering (Fig. 3b, c). At the centimeter and millimeter scale, undulating white sulfur precipitates on siltstones are common along the mainstream course (Fig. 3d). In contrast

TABLE 2. COMPARISON OF PHYSICAL–CHEMICAL PARAMETERS AND WATER COMPOSITION OF THE DIFFERENT LOCALITIES (WITH AND WITHOUT STROMATOLITES) STUDIED

	Eh/100	*EC/1000*	*Temperature*	*Al/100*	*As/100*	*Ca/100*	*Cr/100*	*Cu/10*	*Fe/100*	*Mg/1000*	*Mn/100*	*Ni/100*	p	*Pb/100*	*Si/10*	*Zn/100*	*SO_4/1000*
Sample	*pH*	*mV*	*µS/cm*	*°C*					*mg/L*								
T.S. (P 2003)	3.1	6.48	3.56	18.8	0.58	1.14	1.32	0	0.68	4.37	0.09	0.33	0.61	0	0	2.18	0.49	2.09
T.S. (V 2003)	3.5	6.41	3.81	21.3	0.55	1.44	1.45	0	0.64	5.83	0.09	0.38	0.68	0	0	2.01	0.58	2.33
T. (V 2015)	2.3	7.77	14.59	32.7	19.74	0.04	4.12	0	10.34	7.90	2.55	3.27	3.43	0	0	6.29	0.04	32.17
T. (V 2018)	2.6	5.38	12.41	25.2	15.96	0	4.22	0	9.81	8.52	2.02	2.46	3.75	0	0	1.48	3.24	19.13
T. (V 2004)	2.7	7.87	15.82	22.0	16.14	0.4	4.27	0	12.76	8.42	2.08	2.96	6.28	4.56	0.01	6.68	3.96	24.15
S.T. (V 2004)	2.7	6.48	10.32	32.9	5.45	0.17	3.31	0	9.82	12.42	1.09	0.97	1.70	1.30	0	7.32	2.42	12.79
S.T. (P 2006)	2.5	6.41	9.59	17.2	6.76	0.12	3.18	0	12.93	16.72	1.22	0.99	1.81	0	0	6.86	3.28	13.76
L. (I 2003)	3.2	7.29	1.78	16.8	0.65	0	0.41	0	1.12	0.18	0.10	0.14	0.43	0	0.01	0.77	0.22	1.25
L. (P 2004)	2.8	7.20	2.44	17.7	0.86	0	0.57	0	1.28	0.14	0.11	0.16	0.46	0	0	2.06	0.28	1.40

Samples with the presence of stromatolites: T.S. (P 2003) = Tintillo Santa Rosa (Spring 2003); T.S. (V 2003) = Tintillo Santa Rosa (Summer 2003); T. (V 2015) = Tintillo (Summer 2015); T. (V 2018) = Tintillo (Summer 2018); T. (V 2004) = Tintillo (Summer 2004). Samples without the presence of stromatolites: S.T. (V 2004) = San Telmo (Summer 2004); S.T. (P 2006) = San Telmo (Spring 2006); L. (I 2003) = La Lapilla (Winter 2003); L. (P 2004) = La Lapilla (Spring 2004).
EC = electrical conductivity; Eh = redox potential.

to exposed TIFs, submerged TIFs show a green coloration due to the spotty presence of microbial mats.

The thickness of TIFs varies from a few centimeters up to 50 cm and exhibit a surficial ocher coloration in areas of higher water depth, especially in zones where orange, yellow, and green floating filamentous mats develop. There is a clear yellow to green zonation along the mid-ridges of pools (Fig. 4a). In general, coarser filamentous populations coincide with coarser sediments, whereas finer filamentous mats develop in flat muddy areas. Filaments align in parallel in zones where sedimentary ridges show a regular pattern (Fig. 4b). The occurrence of monotypic yellow filaments in zones of higher turbulence (Fig. 4c) contrasts with pustular green mats developed around a steep relief or inside natural crevices (Fig. 4d).

4.3. Characterization of TIFs

TIFs exhibit a variable texture and variations among brownish, ochre, and dark red colorations. At 25°C, sampled TIFs show an internal pH of 1.36. The macrostructure of TIFs consists of corrugated surfaces and smooth wavy layering of variable thickness (Fig. 5a, b). A fine greenish-silty and porous lamination at the top is followed by a compacted zone with a millimeter-thick reddish lamination (white arrow in Fig. 5c). The TIFs mesostructure shows a crude granular red/ochre lamination (between 0.5 and 2 cm) that becomes evident upon desiccation. The spongy and porous zone exhibits a brownish lamination and a higher content of plant debris at the lower part, especially acicular pine needles (Fig. 5d). TIFs also reflect a preferential granulometry, consisting of coarse silt-fine-sands and, to a lesser extent, coarse and very coarse sand. TIFs incorporate medium to coarse sand in both analyzed samples, unlike nonstromatolitic iron sediments, which exhibits a more regular distribution of particle size (Fig. 6). Petrographic analysis results show a sharp transition between the ochre and brownish coloration (Fig. 7a), followed by a Fe-rich shrub-like porous texture that shows a dendritic fabric with dark red aggregates (Fig. 7a, b). A second TIF sample similar in color and texture shows differences in lamination thickness and dendritic aggregates (Fig. 7d, f). The dendritic fabric is clearly separated from a massive iron precipitation and followed by iron aggregates (Fig. 7f).

At higher resolution, TIFs show three main textures: a porous and spongy zone, followed by a well-developed lamination with irregular margins that alternates with a spongy fabric, and massive and compacted white zones (Fig. 8a). Thrombolitic textures form a clear banding distinguished by their precipitate size, composition, and color. The main microtextures consist of light-gray millimeter-alternating-layers, with a central precipitation zone in lateral continuity, and an upper mosaic precipitation pattern (Fig. 8b, c). The lower area exhibits two distinctive zones, with heterogeneous iron minerals, and a coarser layering associated with a branching pattern of precipitates (Fig. 8d, e). The cyclic presence of gray and white banding with bundles of parallel filaments and precipitates is observed through the scanned profile. Some zones show a composite fabric, represented by an upper banding with a high structural organization, and sharp boundaries among light, gray, dark, and white zones (Fig. 9a). The internal geochemical profile clearly shows fluctuations

FIG. 2. Sedimentary facies in Tintillo AMD. **(a)** Exposed red shales with mineral zonation of former water level (white arrow). **(b)** Sulfur precipitates on lateral flanks as product of geochemical zonation. **(c)** Microbial mats distributed along the ridged pools. **(d)** Typical iron terraces as main sedimentary facies in Tintillo AMD. **(e)** A panoramic view of the Tintillo AMD with onshore vegetation. **(f)** Point bars facies with terracetes and red pools flanked by distinctive ridges (rdg). TIF, terraced iron formation.

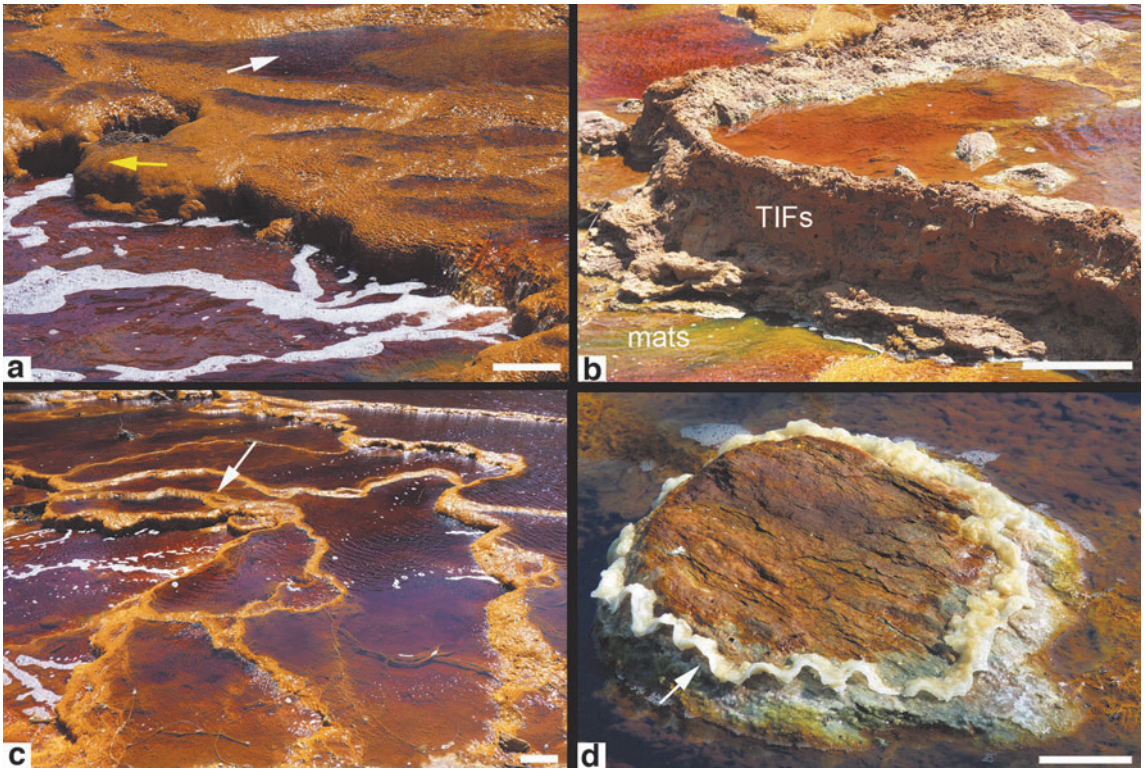

FIG. 3. Terraced-iron formations (TIFs) in the Tintillo river. (TIFs). **(a)** Crenulated terracettes (yellow arrow) with benthic mats and inundated polygonal pools (white arrow). **(b)** Vertical profile of TIFs with surrounding colorful microbial mats. **(c)** Irregular ridges outlining sulfurous pools. **(d)** Curly sulfur precipitation on shales with underlying crustose mats (white arrow).

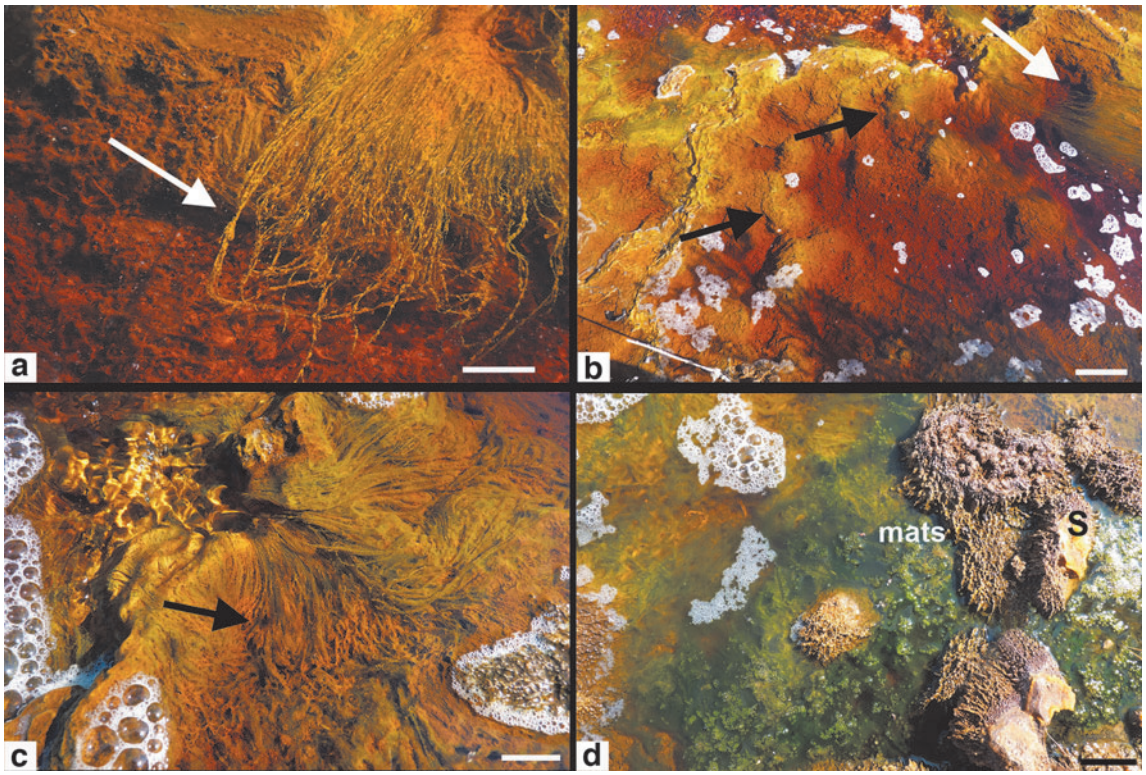

FIG. 4. Representative microbial mats in Tintinillo AMD. **(a)** Macroscopic filamentous microbial mats on a TIF (terrace iron formation) slope (arrow). **(b)** Low-relief ridges (black arrows) with flimsy microbial mats (white arrow). **(c)** Planktonic filamentous mats with a color zonation (arrow). **(d)** Pustular green microbial mats surrounding macroscopic coarser filaments in association with sulfur precipitates (S). Scale bar = 3 cm in **(a, b, c)**.

mainly in SO_3 and FeO (Fig. 9b). Interestingly, chloride, SiO_2, and Al_2O_3 show intermittent variations, but other cations remain relatively constant. Similar textural variations can be observed along the z axis orientation (Fig. 9c).

4.4. Microbial assemblage in TIFs

TIFs show at least four discontinuous layers that contain filamentous microbial mats, mainly composed of long algal filaments and other minor uniseriate filaments (arrow in Fig. 10a). The unbranched filaments formed by short cells have been presumably assigned to *Klebsormidium*. Other long filaments, formed by barrel-shaped cells similar to preakinetes of *Zignema* sp., are frequent (Fig. 10b, c). Some cells show a terminal dichotomous branching (a Y-bifurcation) and a spheroidal protuberance (arrow in Fig. 10b). Filaments are closely associated with diatoms and with brownish precipitates (Fig. 10d). In contrast to the floating microbial mats formed by thick light orange and green filaments, the filaments in TIFs show yellow, white, and brown precipitates among filament intersections. Such precipitates occur as small, euhedral, or irregular yellow minerals that entomb filaments (Fig. 10e). Other precipitates occur as small globular sulfur on filaments, which may exhibit a black or white color (arrows in Fig. 10f). A closer look reveals that barrel-shaped cells (4 μm in diameter) form uniseriate trichomes surrounded by a thin mucilaginous material (Fig. 10g, h). The black entangled filaments with sulfur precipitates are associated with diatoms, which are abundant through the vertical profile of TIFs.

4.5. Mineral–extracellular polymeric substances interaction

Although filamentous morphotypes are a dominant microbiota, pennate frustules are not only well represented, but they occur in close association with mineral precipitates and with extracellular polymeric substances (EPS). Diatoms are conspicuous throughout the vertical profile of TIFs, and they preferentially align on outlining interfaces of the mineral matrix (Fig. 11a). The mineral matrix is composed of radial spherules of schwertmannite $[Fe^{+3}{}_{16}O_{16}(OH)_{12}(SO_4)_2]$ with organic remains in which diatoms are embedded (Fig. 11b–f). It is clear that the density of diatom populations influences the geometry of open spaces inside the mineral matrix (Fig. 11a–c). The EPS seems to promote mineral cohesion and agglutination (Fig. 11e). *Stauroneis kriegeri* is commonly found inside a reticulated mineral matrix (Fig. 11h) and in massive amorphous surfaces (Fig. 11i).

The diatom assemblage includes *Nitzschia aurariae*, *Pinnularia aljustrelica*, *S. kriegeri*, and *Fragilaria* sp. These pennate diatoms form an integral part of the mineral matrix, which contains remains of organic EPS and schwertmannite as the most common mineral (Fig. 12a). TIF upper layers contain interconnected spheroidal radial crystals of schwertmannite (Fig. 12b). *P. aljustrelica*, among others, is closely associated with schwertmannite (Fig. 12c–f). Other small crystals may be attached to cell walls as connecting pads, only on one side (Fig. 12f).

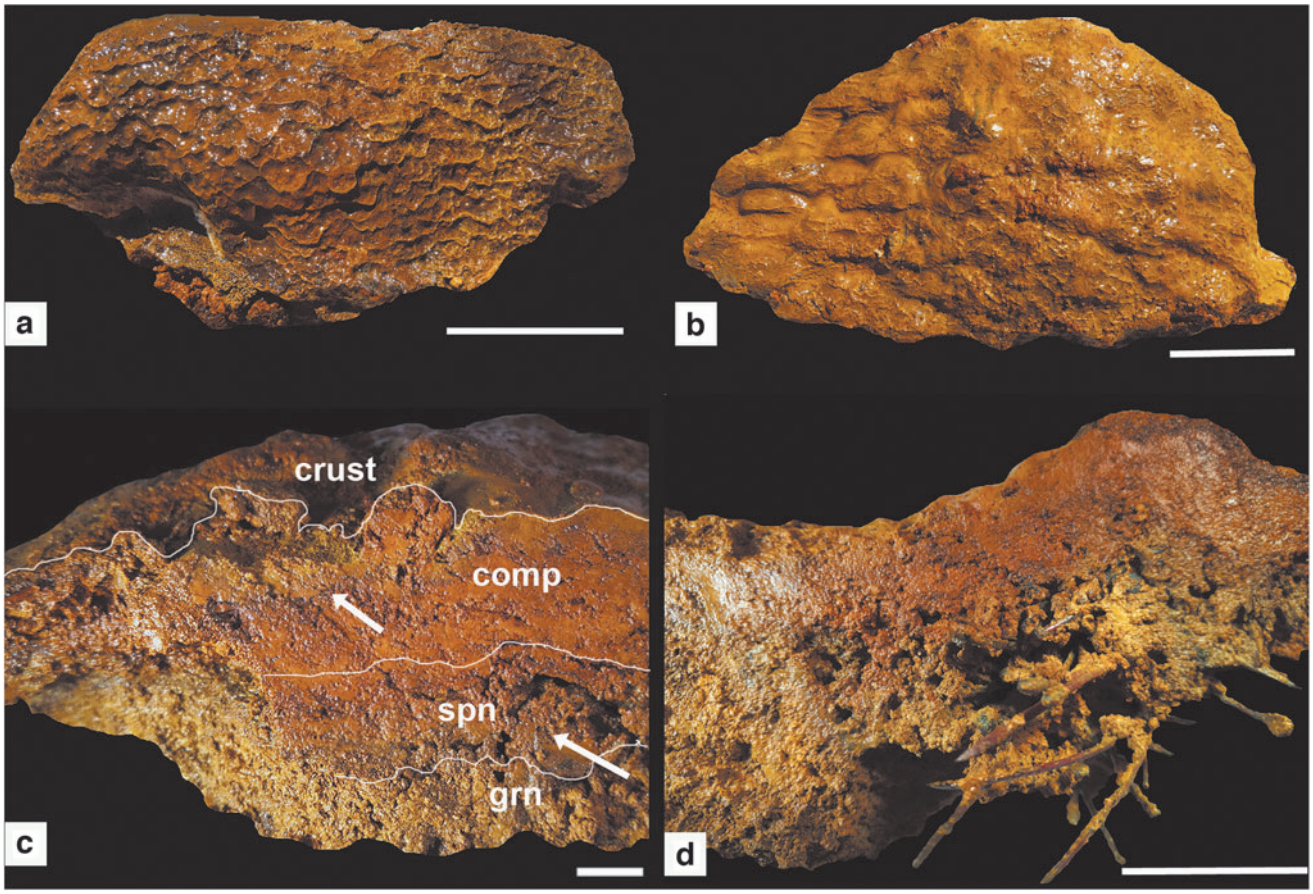

FIG. 5. Mesostructure of sampled TIFs. **(a, b)** Reticulate and crenulated surficial TIFs textures. **(c)** Lamination through the vertical profiles from bottom to top: granular (grn), spongy (spn), and compacted (comp.) layering, covered by a filmy-corrugated crust; arrows show the most fragile zones in TIFs lamination. **(d)** Lateral view of a sampled TIF with a high content of acicular pines. Scale bar in **(a, d)** = 5 cm; in **(b, c)** = 1 cm.

5. Discussion

5.1. The stromatolitic texture of TIFs

The formation of terracettes as a geomorphological feature of riverine systems has been classically assigned to erosion and aggradation. The floodplain can be transformed into a terrace by tectonic, climatic, or human-induced changes that alter the regimen of the river (Gordon and Luna, 1967) where erosional edges are suitable substrates for microbial mats (Gerdes *et al.*, 1994). The high diversity

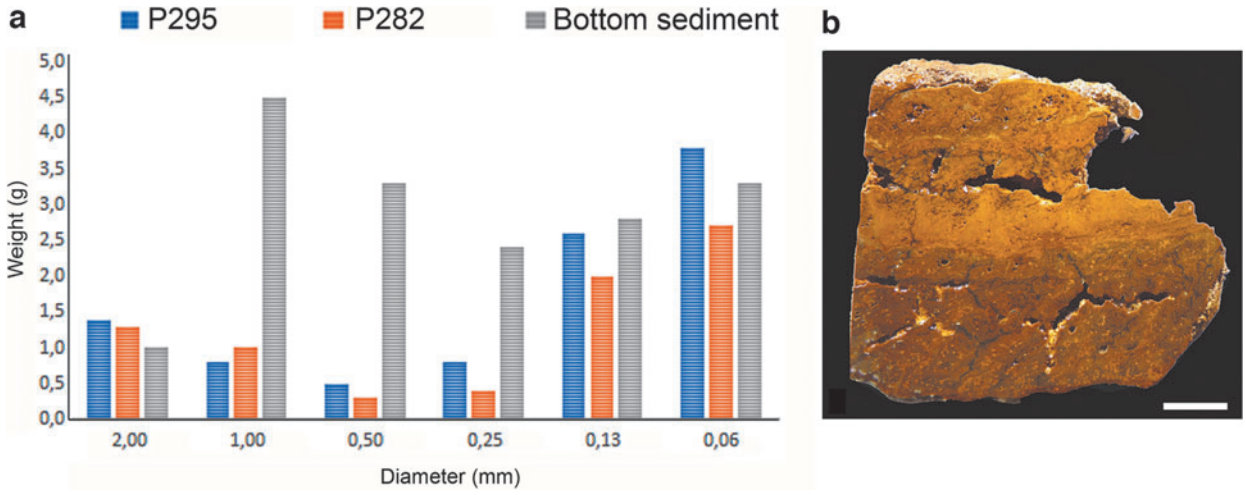

FIG. 6. Grain size distribution in two TIFs (P282 and P295). **(a)** Size grain distribution in the lamination of the iron stromatolites P282 and P292, in comparison with a nonlaminated sediment used as control (bottom sediment). **(b)** TIF lamination in sample 295 with visible color gradations.

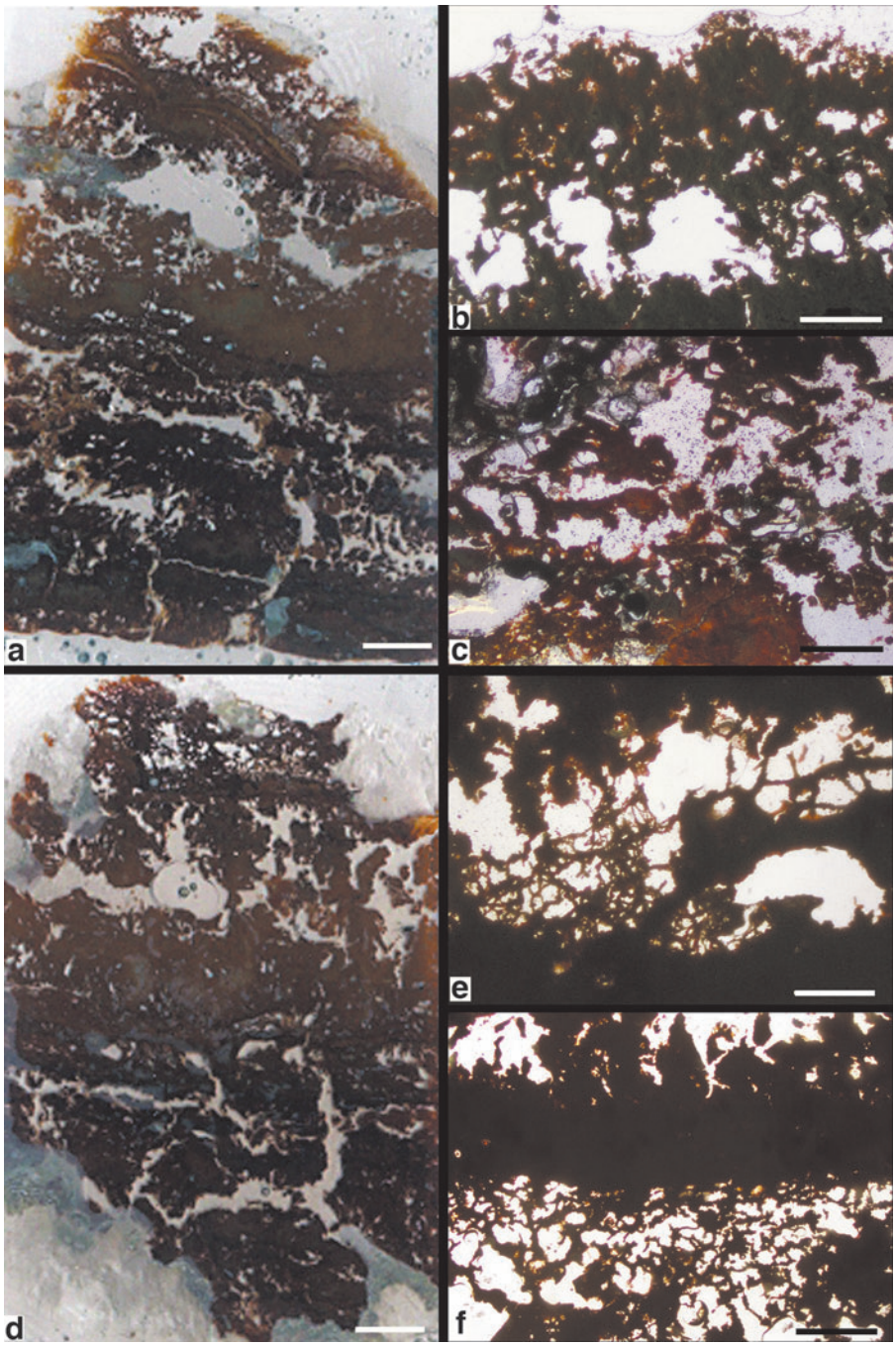

FIG. 7. TIFs petrography. **(a, d)** Petrographic thin sections showing a mesoscale lamination in different colors. **(b, c, e, f)** Reticulate fabrics with radiating textures that alternate with massive and symmetric iron precipitation. Scale bar = 4 mm in **(a, d)**; 500 μm in **(b, c, e, f)**.

of geochemical gradients promotes the colonization of the water–sediment interface by microbial communities. These microecosystems, in turn, accrete and stabilize during erosion, turbulence, and inundation episodes. The increasingly AMD anthropogenic deposits, which unfortunately exhibit an extensive distribution worldwide, are propitious environments for the formation of iron stromatolites. These clastic iron stromatolites are the result of a synergistic effect among clastic input, microbial metabolisms, and fluvial processes that produce similar mineral facies in AMD systems.

A common problem associated with microbial sediments is their classification in genetic and descriptive terms. However, the depositional environment adds another criterion in microbialites. The Tintillo clastic iron stromatolites are unique in their genesis, and therefore, their classification as microbialites is not straightforward. In low-energy settings, TIFs could also be regarded as unlithified microbial mats where mineralogy may dictate the difference between lithified and unlithified mats. Their morphological attributes, such as a millimeter-scale flat-topped crests similar to ripples and a reticulate pattern on crenulated microstructures, are comparable to other ancient siliciclastic surfaces (Porada and Bouougri, 2007). Since TIFs are not discrete structures, but form part of a clastic interface environment formed by chemical iron precipitation (basically, a clastic deposit),

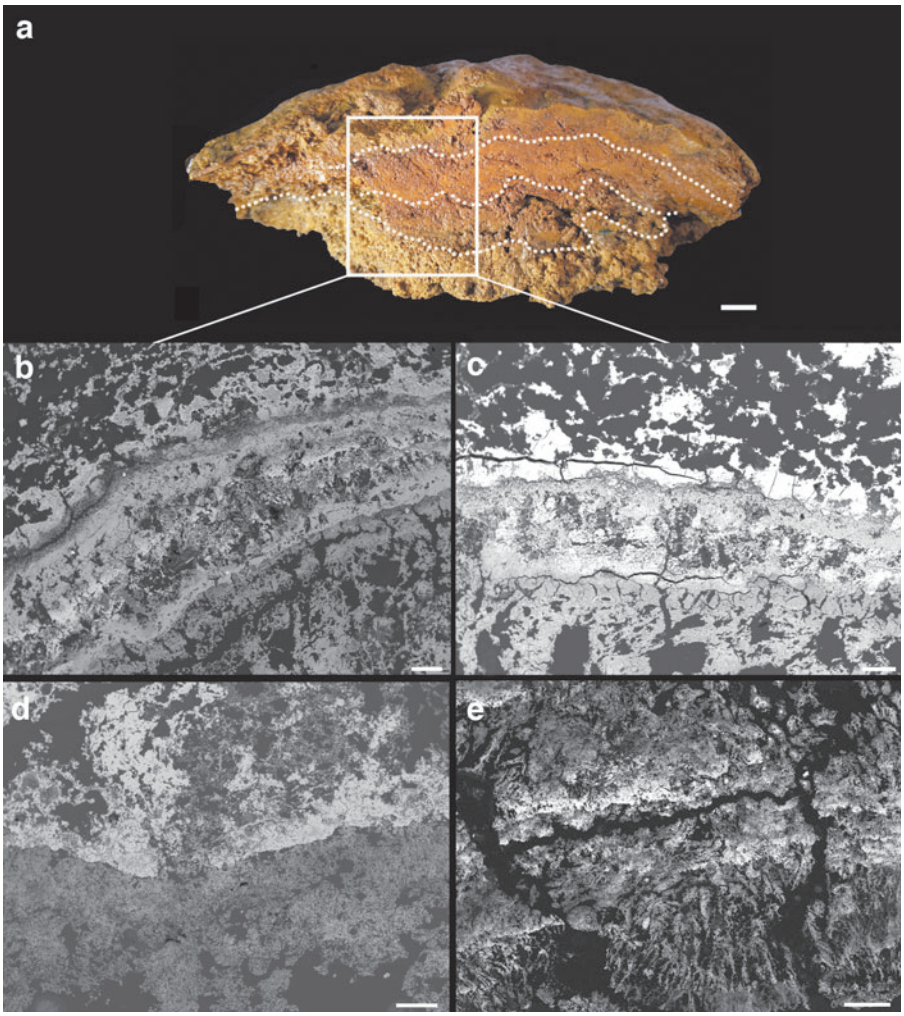

FIG. 8. TIFs microstructure. **(a)** Textural variations in lamination. **(b, c)** Well-defined symmetric lamination blanketed by clotted textures. **(d)** Transitional zones with amorphous iron aggregates in the spongy zone. **(e)** Coarse lamination in the grainy banding with radial bundles of iron precipitates. Scale bar = 1 cm in **(a)**; = 500 μm in **(b–e)**.

they could also be regarded as a laminated example of MISS (microbially induced sedimentary structures), following the criteria given the works of Noffke *et al.* (2003, 2008) and Noffke and Awramik (2013). The debate about the nature of MISS (Davies *et al.*, 2016) highlights the complex interplay between abiotic and biotic factors in the accretion of microbial structures with a well-defined pattern (lamination).

TIFs are characterized by a specific grain-size range formed in siliciclastic environments, under relatively stable hydrodynamic conditions, with seasonal variations within a contaminated river. Because of their lamination, they are reported as clastic iron stromatolites, with precipitation, union, baffling, and trapping processes, but no lithification. As pointed out by Gerdes (2007), many terms reflect similar features (see, for instance, the pioneer terminology in Logan *et al.*, 1974). Under this umbrella, TIFs could be regarded as laminated microbial deposits with a high amount of detrital sediments. Given that TIFs represent modern, although not lithified, potential stromatolites (Krumbein, 1983) and form accretionary structures with a biogenic primary lamination, they could also be fitted into the stromatolites' definition given in the work of Hofmann *et al.* (1999). In modern environments, TIFs may be viewed as products of biologically mediated geochemical gradients that develop a ''stromatolitic'' lamination (*sensu* Kalkowsky, 1908), where nutrients, flow rates, and other critical parameters promote their development (Dodd *et al.*, 2018).

5.2. TIFs and water geochemistry

As observed in Table 2, there is a trend toward a seasonal stability for measured parameters in the studied sampling sites. The concentrations of dissolved elements in Tintillo are very high. For instance, the sodium concentration averaged 29.8 mg/L, but previous results reported a sodium average value of 32.02 and 24.17 mg/L for 2003 and 2004, respectively (Sánchez-España *et al.*, 2007). In the present study, potassium was not detected, but its average values were 1.61 and 0.98 mg/L in 2003 and 2004, respectively (Sánchez-España *et al.*, 2007). The absence of Cl and Br in this and in previous studies of the same localities is clear.

The microtexture of TIFs shows that FeO is the most abundant ion, followed by SO_3, that presents larger variations in abundance along the vertical fabric. SiO_2 also shows large variations, but Al_2O_3 shows variations to a lesser extent. Potassium, magnesium, and calcium show smaller fluctuations in TIFs. As presented in Table 2, waters surrounding TIFs also contain a significantly higher content of most measured cations. This cation enrichment in TIFs probably elicits bacterial ion pumps and multiple biogeochemical

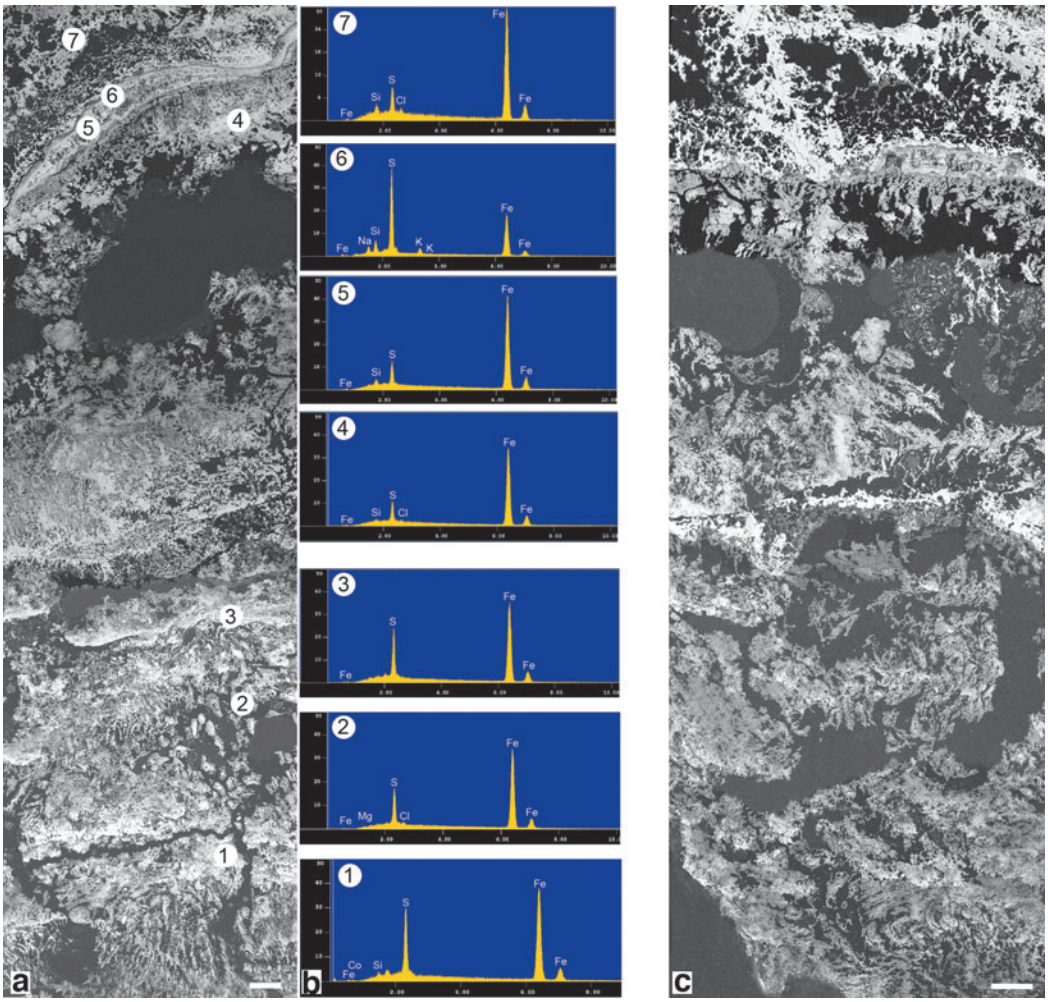

FIG. 9. Petrographic compositional map of TIFs. **(a)** Vertical section of iron stromatolites (TIFs) showing alternate lamination and clotted abric with branching iron aggregates. Encircled numbers correspond to chemical determinations in **(b)**. **(b)** Chemical variation of microtextures in TIFs showed in **(a)**. **(c)** Cross section of TIF sample in the *z* axis, which shows interlayering of massive iron aggregates and precipitation bundles; a well-defined lamination and clotted texture is visible at the upper zone. Scale bar in **(a, b)** = 100 μm.

pathways to cope with high metal concentrations. Such adaptive microbial responses further increase the complexity between abiotic and biotic factors in AMD.

The EC is clearly different in localities with and without TIFs development. TIFs show a relatively high EC (Table 2), which is due to elements such as Fe, Mg, Zn, Ca, Al, and sulfates. A higher EC may also favor the development of lamination due to a rapid current flow through the biofilm. However, other stromatolites samples, as shown in Table 2 [samples T.S.R. (P 2003) and T.S.R. (V 2003)], display lower EC values and a higher pH, but they also exhibit a relatively smaller size.

These results also show that stream waters at Tintillo AMD present anomalies in the distribution and sequestration of toxic metals. Apparently, TIFs grow under a high mineral selectivity, since surrounding waters show higher concentrations of metal in comparison with waters where TIFs are absent (Table 2). This finding may also suggest that floating microbial mats may capture and provide sequestration sites for toxic metals. Metal concentration in AMD systems changes seasonally but is strongly dependent on the proximity of tailings piles and abandoned mines (Campaner *et al.*, 2014); it is also a function of depth (Wielinga *et al.*, 1999). As observed in Fig. 6, TIFs preferentially accumulate either very large or very small grains in their lamination. This attribute may be related to the microbial population density and the quantity of organic matter, which may promote trapping and binding of some grains more than others. The accretion of mats by precipitation, trapping, and binding has been reported in similar TIFs structures (Hasiotis and Brake, 2019).

5.3. Diatoms EPS and schwertmannite

The present study provides direct evidence of the interaction among diatoms as *P. aljustrelica* and *N. aurariae*, EPS, and schwertmannite (Figs. 11 and 12). Recent literature has documented the role of microbial EPS on mineralization processes during accretion of stromatolites and a prominent role for diatoms (Brake *et al.*, 2004, 2014;

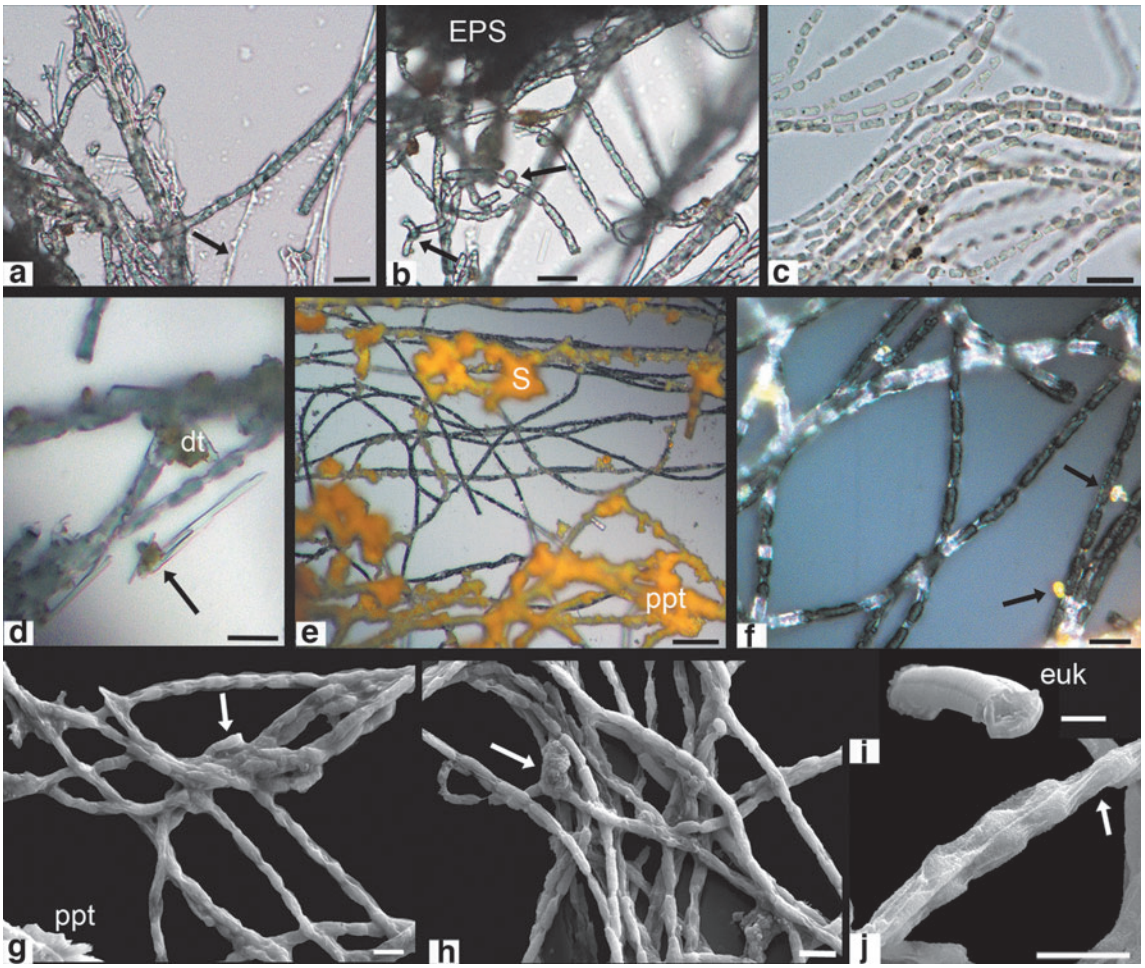

FIG. 10. Microbial filaments in Tintillo TIFs. **(a)** Uniseriate filaments similar to *Klebsormidium* sp. Other small white filaments are also visible (arrow). **(b)** Algal filaments with a Y-bifurcation and spheroidal protuberance (arrows). **(c)** Long *Klebsormidium*-like filaments. **(d)** Associated diatoms (dt) and granular precipitates (arrow). **(e)** Black filaments entombed by yellow sulfur (S) precipitates (ppt). **(f)** Black and white filaments, with and small yellow precipitates (arrows). **(g, h)** SEM of filaments with agglutinated precipitates (ppt) at junctions (arrows). **(i)** A solitary protist. **(j)** Uniseriate filaments surrounded by an irregular sheath (arrow). Scale bar in **(a–d, f)** = 10 μm; in **(e)** = 50 μm; in **(g–i)** = 20 μm; in **(j)** = 5 μm. SEM, scanning electron microscope.

Hasiotis and Brake, 2019). The acidophilic diatom *P. aljustrelica* has been found to thrive in the conspicuous biofilms at the Río Tinto and other related rivers from the IPB (Amaral-Zettler, 2012; Luís *et al.*, 2012, 2016). The close relationship between schwertmannite and EPS suggests an active role of diatoms in precipitation. These microbial–mineral interactions not only influence mineral transformations (Bao *et al.*, 2018) but may also increase the porosity of sediments.

The precipitation of schwertmannite, a common metastable mineral found in extremely acidic environments, is the product of abiotic reactions (Sánchez-España *et al.*, 2007, 2011), but field and experimental evidence suggests that microbial populations may enhance its nucleation and stability. Furthermore, the removal of toxic metals may be naturally enhanced by schwertmannite and ferrihydrite, depending on the pH (Carlson *et al.*, 2002; Sánchez-España *et al.*, 2006, 2011). The secretion of cohesive EPS by microbial biofilms also influences sediment entrainment, transport rate, and dimensions, even where thick surficial biofilms and microbial mats are not present (Garwood *et al.*, 2013; Malarkey *et al.*, 2015).

In general, AMD environments exhibit not only mineral–microbial interactions but also a notable diversity of morphologically diverse microbial mats promoted by steep geochemical gradients (Blackmore *et al.*, 2018). Most organisms, except euryhaline species, are unable to cope with environmental extremes in AMD settings, and thus, bacterial proliferation increases. The occurrence of *Acidithiobacillus ferrooxidans*, *Acidithiobacillus thiooxidans*, *Leptospirillum ferriphilum*, *Leptospirillum ferrooxidans*, *Gallionella ferruginea*, *Thermoplasmata*, *Ferrovum*, *Sulfobacillus*, and *Thiobacillus* has been described from AMD around the world (Benner *et al.*, 2000; Bruneel *et al.*, 2006; Sánchez-España *et al.*, 2007; Goltsman *et al.*, 2009; Schippers *et al.*, 2010; Korehi *et al.*, 2013; Williams *et al.*, 2017; Bomberg *et al.*, 2019), including eubacteria from highly acidic environments (Benner *et al.*, 2000; Korehi *et al.*, 2013; Johnson and Aguilera, 2016; Johnson and Quatrini, 2016). Molecular studies from acid waters have

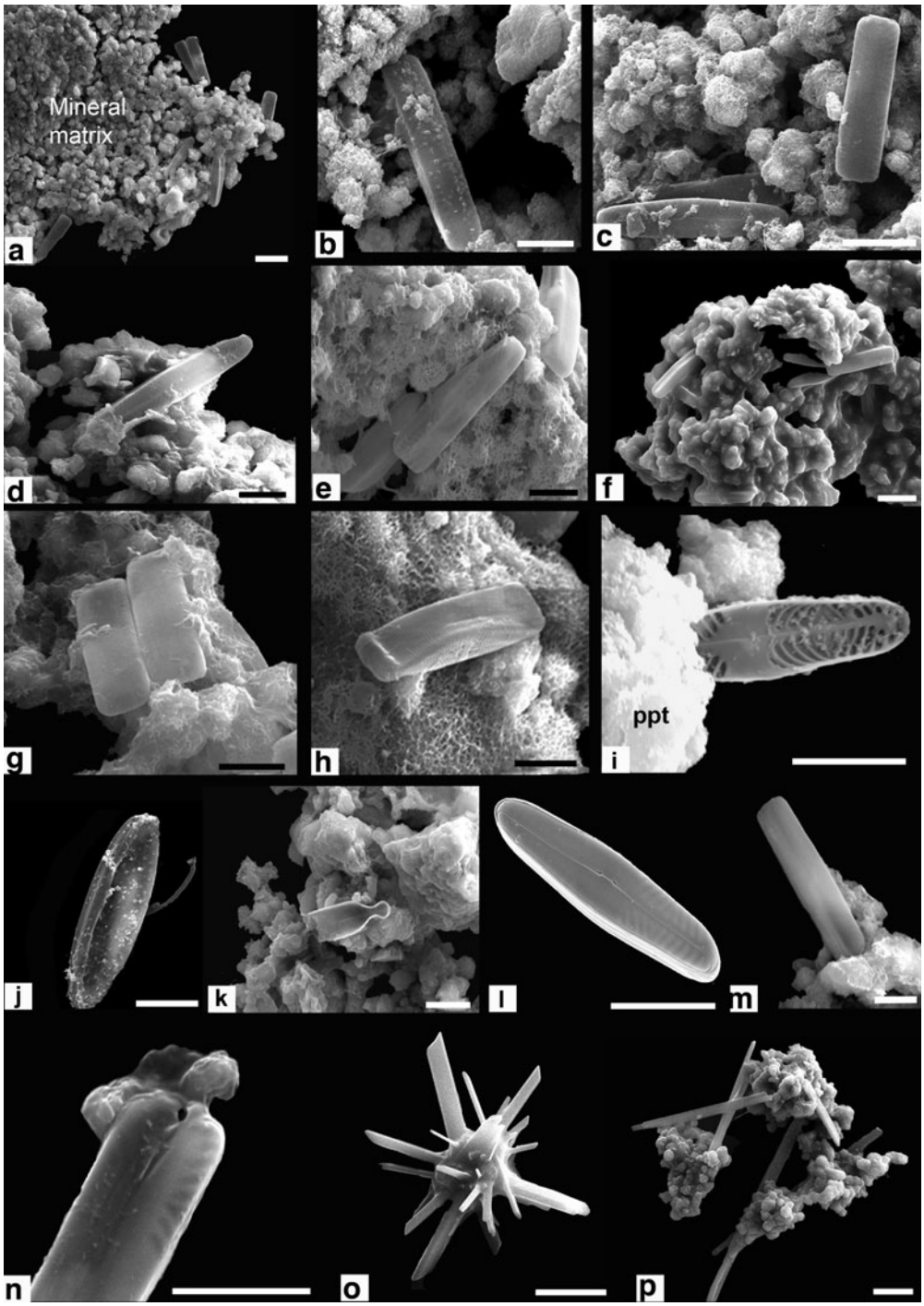

FIG. 11. TIFs 3D microstructure. **(a, b)** Embedded diatom frustules inside the mineral matrix. **(c–g)** Clusters of spheroidal schwermannite (Schw) with pennate diatoms. **(h)** *Stauroneis kriegeri* lying on schwermannite. **(i)** *Pinnularia aljustrelica* inside an amorphous mineral precipitate (ppt). **(j)** *Nitzchia aurariae*. **(k)** *Fragillaria* sp. **(l)** *P. aljustrelica.* **(m, n)** Crystalline aggregates on diatom frustules. **(o)** Radial acicular aggregates glued by organic remains. **(p)** Clusters of schwermannite around acicular precipitates. Scale bar in **(a, f, o, p)** = 10 μm; in **(b–e, g–n)** = 5 μm. 3D, three-dimensional.

shown that they are enriched in filamentous algae, cyanobacteria, diatoms, as well as protozoans and eukaryotic communities across all distinct microhabitats (Mesa *et al.*, 2017). The most common phototrophs correspond to green microalgae (Dean *et al.*, 2019). Among eukaryotes, green algae, diatoms, and euglenoids are among the most represented, but ciliates, cercozoans, rotifers, amoebas, stramenopiles, and fungi have also been reported (Packroff and Woelfl, 2000; Brake *et al.*, 2001, 2004; Aguilera *et al.*, 2007; Rawlings and Johnson, 2009; Aguilera, 2013; Massocato, 2018). Open-air water samples contain diverse eukaryotes from the fungal group Alveolata, Stramenopiles, and Opisthokonta.

Pine needles are another essential component of TIFs, not only in terms of size and textures but also as an additional

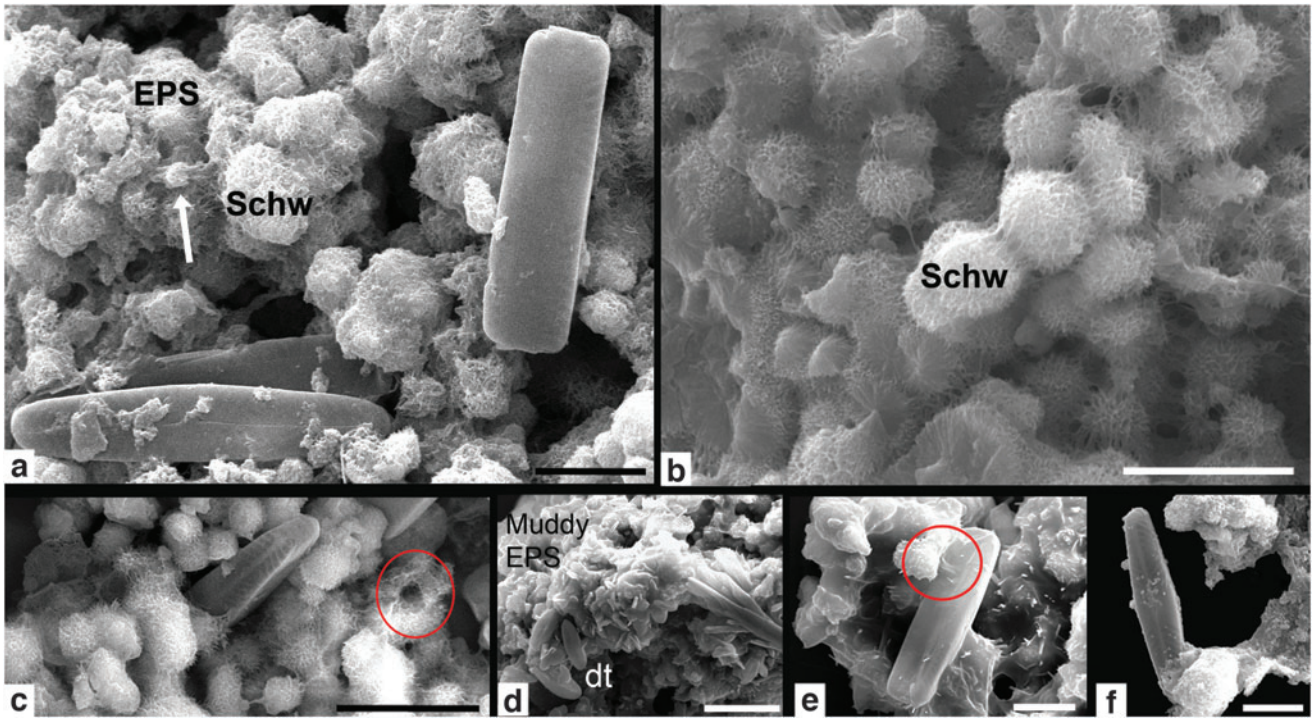

FIG. 12. SEM micrographs of diatoms inside iron stromatolites. **(a, b)** Diatoms and EPS remains (arrow in **a**), embedded inside the mineral matrix of schwermannite (Schw). **(c)** Diatoms inside voids and internal pores (red circle). **(d)** Crystalline mineral clusters with diatoms and muddy EPS remains. **(e, f)** Association between diatoms and schwermannite (red circle). Scale bar in **(a, b, e)** = 5 μm; in **(c, d, f)** = 10 μm. EPS, extracellular polymeric substances.

source of organic matter and carbon, as corroborated in this work. The presence of an ochre colloidal mixture (mostly schwertmannite) and green algal mats, mainly composed of *Euglena mutabilis* and pine needle debris (LeBlanc *et al.*, 1996; Sánchez-España *et al.*, 2005c), is common in AMD environments but was not detected inside the sampled TIFs, probably due to marked seasonal changes in its population (Hasiotis and Brake, 2019).

5.4. Analogues of Archean Earth

Clastic iron stromatolites from AMD may be used as valuable modern analogues to infer sedimentary environments, before and after the Global Oxygenation Event (GOE). AMD systems may represent modern analogues of Paleoproterozoic continental surfaces during the Mesoproterozoic times, just when the pre-Cambrian BIFs were deposited (Brake *et al.*, 2002, 2014; Parenteau and Cady, 2010; Westall *et al.*, 2015; Kanellopoulos *et al.*, 2019). Before the GOE, pyrite would accumulate as placer deposits on continental surfaces during the Archean (Johnson, 2014). Habitats that resembled AMD probably existed for billions of years. Once oxygen became available, the oxidation of pyrite promoted the eventual sedimentary riverine transport that delivered iron and sulfate to the oceans (Havig *et al.*, 2017).

BIFs have also been interpreted as sedimentary files of transient atmospheric conditions, during the Archean. Paleoproterozoic oceans were rich in Fe(III) (Poulton and Canfield, 2011) under anoxic atmospheric conditions with widespread surficial oxygenation at archean ocean margins (Kendall *et al.*, 2010; Konhauser *et al.*, 2011). For instance, the Biwabik BIFs (1.85 My) are the most extensive and economically important iron deposits worldwide, and they were abundant at the end of the Archean. Other Precambrian low-pH environments generated by volcanism may have been crucial for the origin of life on Earth (Phoenix *et al.*, 2006).

5.5. Natural bioremediation through geomicrobiology

Several years of mining in the IPB, one of the most extensive metal sulfide ore deposits regions in the world (Sáez *et al.*, 1999; Johnson, 2014), has resulted in enormous metal-rich wastes and eventual ecosystem degradation by AMD of the main river systems that run over the IPB, which include the Tinto and the Odiel rivers (Grande *et al.*, 1999; Nieto *et al.*, 2007; Sarmiento *et al.*, 2008, 2018; Shuster *et al.*, 2017). When AMD sulfides are exposed to oxygen and water, they dissolve and produce H_2SO_4 and Fe(II) (Nordstrom and Southam, 1997). These reactive chemical species acidify as the stream flows down and the pH decreases. When the pH drops to 3.5 or even 2.5, the toxicity and metal mobility are higher (Sánchez-España *et al.*, 2005a). This toxicity creates, in turn, new niches for acidophiles (Konhauser, 2007; Johnson and Quatrini, 2016), such as *A. ferrooxidans* or *L. ferrooxidans* (Rohwerder *et al.*, 2003). Since mineral matrices provide suitable substrate for bacterial colonization, AMD hold great potential in bioremediation (Verb *et al.*, 2001; Chockalingam and Subramanian, 2006; Florence *et al.*, 2016; Byrne *et al.*, 2018; Dean *et al.*, 2019) and biopharmacy (Oberholster *et al.*, 2013; Ayangbenro *et al.*, 2018). Additionally, the bioleaching process of some toxic metals is a

common phenomenon in AMD systems (Johnson, 2014). In fact, biosorption techniques employ the synergy between microalgae that supply organic matter and heterotrophs as CO_2 suppliers (Rohwerder *et al.*, 2003; Rawlings and Johnson, 2009; Florence *et al.*, 2016; Abinandan *et al.*, 2018). The biological removal of toxic metals by *Ferrovum myxofaciens* through biosorption (Hedrich *et al.*, 2011) and the biosorption of Ni(II) and Pb(II) by fungal biomass (Aytar *et al.*, 2014) are good examples. Biological strategies to cope with heavy metals found in AMD microorganisms include efflux-mediated metal transport, metal exclusion, intracellular and extracellular sequestration, and enzymatic detoxification (Denef *et al.*, 2010). *E. mutabilis* shows a metal-fixing behavior in the formation of accretionary organic sedimentary structures in AMD settings (Brake *et al.*, 2002, 2004, 2014). The transparency of the same filaments in conjunction with black and yellow colorations (Fig. 10) suggests an active process of bioleaching and biosorption for sulfur precipitates at the periplasmic membrane. The unidentified filament that presumably takes sulfur from the surroundings is similar in shape, size, and behavior to the small filaments reported in the work of Mori *et al.* (2017), who identified them as a novel Eubacterial genus (*Acidithrix*). This study also confirms a differential sulfur precipitation that is mainly concentrated at filament junctions and in specific locations (Fig. 10g–j).

5.6. Astrobiological implications

Modern microbial colonization of such extreme environments is a consequence of the biogeochemical gradients generated through the stream channel. The occurrence of iron stromatolites as TIFs in Tintillo is not only scarce but also peculiar in their precipitation and origin. Because they provide new sedimentary, mineralogical, and chemical biosignatures, microbial consortia inhabiting highly acidic extreme environments hold a great industrial potential in bioremediation and biopharmacology; more importantly, they are also recognized as excellent analogues of ancient Mars environments (Amils *et al.*, 2007, Amils and Fernández-Remolar, 2014). The present study shows that a broad spectrum of textures and colors, enhanced by sediment topology, is also an empirical indication of sharp geochemical gradients.

TIFs are astrobiologically relevant because of their similarity with geological structures found on Mars (Brake *et al.*, 2004; Fernández-Remolar and Knoll, 2008; Loiselle *et al.*, 2018). For instance, the exposed rocks in the Meridiani Planum suggest arid, acidic, and oxidizing environmental conditions, which probably preserve mineralogical biosignatures (Fernández-Remolar *et al.*, 2005; Knoll *et al.*, 2005; Amils *et al.*, 2007; Fernández-Remolar and Knoll, 2008; Loiselle *et al.*, 2018). Furthermore, the relatively high amount of sulfate and hematite may indicate the presence of schwertmannite on the Red Planet (Des Marais *et al.*, 2008; Bishop *et al.*, 2015). Hydrated minerals and sulfates are also common on the Valles Marineris of Mars surface (Kaplan *et al.*, 2016). Hence, Tintillo TIFs represent an excellent modern analogue of BIFs and a promising extreme environment to search for microbial biosignatures. Life in extreme environments enables us to understand the versatility of metabolisms in prokaryotes and explore for possible life beyond Earth (Westall *et al.*, 2013; Preston *et al.*, 2020).

The diversity of minerals, microorganisms, biofabrics, and geomorphological structures in the Tintillo AMD system provides multiple scales of observation with which to identify biosignatures, some of which are the result of pervasive interaction between abiotic and biotic factors (Fig. 13).

There is a continuous need to develop criteria and standards from microscopic to planetary scales in Astrobiology (Cady *et al.*, 2003; Des Marais *et al.*, 2008; Hays *et al.*, 2017) to facilitate examination and identification of sedimentary contexts across multiple spatial and temporal scales, in particular to distinguish abiotic from biotic substances, objects, and patterns (Chang *et al.*, 2019). The recognition of biogenic landforms and a lateral comparative

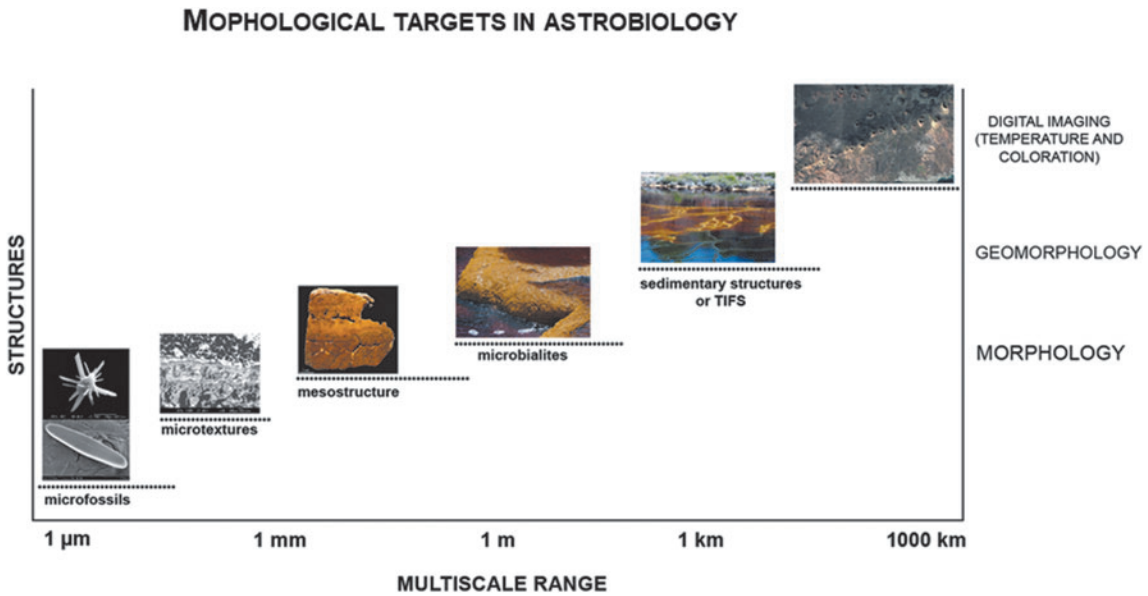

FIG. 13. Multiscale comparison of morphological targets relevant in astrobiology (modified from McKay, 1992).

assessment of diverse terrestrial environments provides guidance for future space exploration (Ibarra and Corsetti, 2016; Corenblit *et al.*, 2019). Under the rationale that complexity arises from gradients (Spitzer *et al.*, 2015), large-scale attributes such as morphology and complexity patterns are still needed to delineate the astrobiological quest, which may include extreme environmental interfaces as well as large-scale geological processes.

The main challenge in Astrobiology is the recognition of life as we know it, but also as we do not expect it. This implies that geological environments may abound in geochemical gradients that produce gradational colors and morphological patterns. Other challenges faced by astrobiology include the cost of high-resolution equipment and the robotic exploration time of targeted sites that store, retrieve, analyze, and visualize spatial data in Geographic Information System (GIS) applications and map services (Macfarlane *et al.*, 2018; McKay, 2020). Such large-scale attributes as topography, geomorphology, and coloration that reflect geochemical gradients, temperature, or geochemical gradients can be assessed by GIS. Since a morphological recognition precedes topographic and cartographical studies, and this mega-scale recognition precedes the macro-, meso-, and microanalysis for characterization of biosignatures, a strong emphasis should be placed on morphological approaches in studies derived from extreme environments.

Acknowledgments

We thank the kind suggestions from Prof. Stepko Golubic and from one anonymous Reviewer. We are very thankful for all the professional help and kindness of the Astrobiology Editorial Team. We also thank Prof. Gloria Arjona (Caltech) for academic editing. The authors are very grateful to Prof. Eduardo Mayoral for fruitful discussions and field photography.

Author Disclosure Statement

The authors declare that the research was conducted in the absence of any commercial or financial relationships that could be construed as a potential conflict of interest.

Funding Information

This paper was partially supported by Research Project CGL2015-66835-P of the Ministerio de Ciencia e Innovación of Spain. Publication costs were partially covered by UANL-PAICyT CN1246-20.

References

Abinandan S, Subashchandrabose SR, Venkateswarlu K, *et al.* (2018) Microalgae–bacteria biofilms: a sustainable synergistic approach in remediation of acid mine drainage. *Appl Microbiol Biotechnol* 102:1131–1144.

Aguilera A (2013) Eukaryotic organisms in extreme acidic environments, the Río Tinto Case. *Life* 3:363–374.

Aguilera A, Manrubia SC, Gómez F, *et al.* (2006) Eukaryotic community distribution and their relationship with the water physicochemical parameters in an extreme acidic environment, Río Tinto (SW, Spain). *Appl Environ Microbiol* 72: 5325–5330.

Aguilera A, Zettler E, Amaral-Zetler L, *et al.* (2007) Distribution and seasonal variability in the benthic eukaryotic community of Río Tinto (SW, Spain), an acidic, high metal extreme environment. *Syst Appl Microbiol* 30:531–546.

Alçiçek H, Bülbül A, Brogi A, *et al.* (2018) Origin, evolution and geothermometry of thermal waters in the Gölemezli geothermal field, Denizli Basin (SW Anatolia, Turkey). *J Volcanol Geotherm Res* 349:1–30.

Amaral-Zettler LA (2012) Eukaryotic diversity at pH extremes. *Front Microbiol* 3:1–17.

Amils R and Fernández-Remolar D (2014) The Ipbsl Team. Río Tinto: a geochemical and mineralogical terrestrial analogue of Mars. *Life* 4:511–534.

Amils R, González-Toril E, Fernández-Remolar D, *et al.* (2007) Extreme environments as Mars terrestrial analogues: the Rio Tinto case. *Planet Space Sci* 55:370–381.

Anderson EW (1972) Terracettes: a suggested classification. *Royal Geogr Soc* 4:17–20.

Awramik SM (1977) Paleobiology of stromatolites. In *Chemical Evolution of the Early Precambrian*, edited by C Ponnamperuma, Academic Press, New York, pp 111–131.

Ayangbenro AS, Olanrewaju OS, and Babalola OO (2018) Sulfate-reducing bacteria as an effective tool for sustainable acid mine bioremediation. *Front Microbiol* 9:1986.

Aytar P, Gedikli S, Buruk Y, *et al.* (2014) Lead and nickel biosorption with a fungal biomass isolated from metal mine drainage: Box–Behnken experimental design. *Int J Environ Sci Technol* 11:1631–1640.

Bao Y, Guo C, Lu G, *et al.* (2018) Role of microbial activity in Fe(III) hydroxysulfate mineral transformations in an acid mine drainage-impacted site from the Dabaoshan Mine. *Sci Total Environ* 616–617:647–657.

Barbieri R and Cavalazzi B (2018) Microterracettes in Sabkha Oum Dba (Western Sahara, Morocco): physical and biological interactions in the formation of a surface micromorphology. *Astrobiology* 10:1351–1367.

Benner SG, Gould WD, and Blowes DW (2000) Microbial populations associated with the generation and treatment of acid mine drainage. *Chem Geol* 169:435–448.

Bird LJ, Bonnefoy V, and Newman DK (2011) Bioenergetic challenges of microbial iron metabolisms. *Trends Microbiol* 19:330–340.

Bishop JL, Murad E, and Dyar MD (2015) Akaganéite and schwertmannite: spectral properties and geochemical implications of their possible presence on Mars. *Am Mineral* 100: 738–746.

Blackmore S, Vriens B, Sorensen M, *et al.* (2018) Microbial and geochemical controls on waste rock weathering and drainage quality. *Sci Total Environ* 640–641:1004–1014.

Bomberg M, Mäkinen J, Salo M, *et al.* (2019) High diversity in iron cycling microbial communities in acidic iron-rich water of the Pyhäsalmi Mine, Finland. *Geofluids* 2019:7401304.

Brake SS, Dannelly HK, Connors KA, *et al.* (2001) Influence of water chemistry on the distribution of an acidophilic protozoan in an acid mine drainage system at the abandoned Green Valley coal mine, Indiana, USA. *Appl Geochem* 16:1641–1652.

Brake SS, Hasiotis ST, Dannelly HK, *et al.* (2002) Eukaryotic stromatolite builders in acid mine drainage: implications for Precambrian iron and oxygenation of the atmosphere? *Geology* 30:599–602.

Brake SS, Hasiotis ST, and Dannelly HK (2004) Diatoms in acid mine drainage and their role in the formation of iron-rich stromatolites. *Geomicrobiol J* 21:331–340.

Brake SS, Arango I, Hasiotis ST, *et al.* (2014) Spatial and temporal distribution and characteristics of eukaryote-dominated microbial biofilms in an acid mine drainage environment: implications for development of iron-rich stromatolites. *Environ Earth Sci* 72:2779–2796.

Brown JF, Jones DS, Mills DB, *et al.* (2011) Application of a depositional Facies model to an Acid Mine Drainage site. *Am Soc Microbiol J* 77:545–554.

Bruneel O, Duran R, Casiot C, *et al.* (2006) Diversity of microorganisms in Fe-As-rich acid mine drainage waters of Carnoulès, France. *Appl Environ Microbiol* 72:551–556.

Buick R, Dunlop JSR, and Groves DI (1981) Stromatolite recognition in ancient rocks: an appraisal of irregular laminated structures in an early Archean chert barite unit from North Pole, Western Australia. *Alcheringa* 5:161–181.

Burgos WD, Borch T, Troyer LD, *et al.* (2012) Schwertmannite and Fe-oxides formed by biological low-pH Fe(II) oxidation versus abiotic neutralization: impact on trace metal sequestration. *Geochim Cosmochim Acta* 76:29–44.

Byrne P, Hudson-Edward K, Bird G, *et al.* (2018) Water quality impacts and river system recovery following the 2014 Mount Polley mine tailings dam spill, British Columbia, Canada. *Appl Geochem* 91:64–74.

Cady SL, Farmer JD, Grotzinger JP, *et al.* (2003) Morphological biosignatures in the search for life on Mars. *Astrobiology* 3:351–368.

Campaner VP, Luiz-Silva W, and Machado W (2014) Geochemistry of acid mine drainage from a coal mining area and processes controlling metal attenuation in stream waters, southern Brazil. *Anais Acad Bras Ciencias* 86:539–554.

Canfield DE, Rosing MT, and Bjerrum C (2006) Early anaerobic metabolisms. *Philos Trans R Soc B Biol Sci* 361:1819–1834.

Caraballo MA, Sarmiento AM, Sánchez-Rodas D, *et al.* (2011) Seasonal variations in the formation of AL and SI rich FE-stromatolites in polluted acid mine drainage of Agua Agria creek (Tharsis, SW Spain). *Chem Geol* 284:97–104.

Carlson L, Bigham M, and Schwertm U (2002) Scavenging of As from acid mine drainage by schwertmannite and ferrihydrite: a comparison with synthetic analogues. *Environ Sci Techol* 36:1712–1719.

Cavalazzi B, Barbieri R, Gomez F, *et al.* (2019) The Dallol geothermal area, northern Afar (Ethiopia)—an exceptional planetary field analog on Earth. *Astrobiology* 19:553–578.

Chang MA, Hinman NW, Potter-McIntyre SL, *et al.* (2019) Deciphering biosignatures in planetary contexts. *Astrobiology* 19:1075–1102.

Chauhan DS (1979) Phosphate-bearing stromatolites of the Precambrian Aravalli phosphorite deposits of the Udaipur region, their environmental significance and genesis of phosphorite. *Precambrian Res* 8:95–126.

Chockalingam E and Subramanian S (2006) Studies on removal metal ions and sulphate reduction using rice husk and *Desulfotomaculum nigrificans* with reference to remediation of acid mine drainage. *Chemosphere* 62:699–708.

Corenblit D, Darrozes J, Julien F, *et al.* (2019) The Search for a signature of Life on Mars: a biogeomorphological approach. *Astrobiology* 19:1279–1291.

Davies NS, Liu AG, Gibling MR, *et al.* (2016) Resolving MISS conceptions and misconceptions: a geological approach to sedimentary surface textures generated by microbial and abiotic processes. *Earth Sci Rev* 154:210–246.

Dean AP, Hartley A, McIntosh OA, *et al.* (2019) AMD 2-metabolic adaptation of a *Chlamydomonas acidophila* strain isolated from acid mine drainage ponds with low eukaryotic diversity. *Sci Total Environ* 647:75–87.

Denef VJ, Mueller RS, and Banfield JF (2010) AMD biofilms: using model communities to study microbial evolution and ecological complexity in nature. *ISME J* 4:599–610.

Des Marais DJ, Nuth JA, Allamandola L, *et al.* (2008) The NASA Astrobiology Roadmap. *Astrobiology* 8:715–730.

Dodd C, Anderson C, Perissinotto R, *et al.* (2018) Hydrochemistry of peritidal stromatolite pools and associated freshwater inlets along the Eastern Cape coast, South Africa. *Sedim Geol* 373:163–179.

Fernández-Remolar DC, Rodríguez N, Gómez F, *et al.* (2003) Geological record of an acidic environment driven by iron hydrochemistry: the Tinto River system. *J Geophys Res* 108: 5080.

Fernández-Remolar DC, Morris RV, Gruener JF, *et al.* (2005) The Rio Tinto Basin, Spain: mineralogy, sedimentary geobiology, and implications for interpretation of outcrop rocks at Meridiani Planum, Mars. *Earth Planet Sci Lett* 240: 149–167.

Fernández-Remolar DC and Knoll AH (2008) Fossilization potential of iron-bearing minerals in acidic environments of Rio Tinto, Spain: implications for Mars exploration. *Icarus* 194:72–85.

Florence K, Sapsford DJ, Johnson DB, *et al.* (2016) Iron-mineral accretion from acid mine drainage and its application in passive treatment. *Environ Technol* 37:1428–1440.

Fouke BW, Farmer JD, Des Marais DJ, *et al.* (2000) Depositional facies and aqueous-solid geochemistry of travertine-depositing hot springs (Angel Terrace, Mammoth Hot Springs, Yellowstone National Park, USA), United States. *J Sed Res* 70:565–585.

Gao SM, Schippers A, Chen N, *et al.* (2020) Depth-related variability in viral communities in highly stratified sulfidic mine tailings. *Microbiome* 8:89.

Garwood JC, Hill PS, and Law BA (2013) Biofilms size sorting of fine sediments during erosion in intertidal sands. *Estuar Coast* 36:1024–1036.

Gavrilov SN, Korzhenkov AA, and Kublanov IV (2019) Microbial communities of polymetallic deposits' acidic ecosystems of continental climatic zone with high temperature contrasts. *Front Microbiol* 10:1573.

Gerdes G (2007) Chapter 2. Structures left modern microbial mats in their host sediments. In *Atlas of Microbial Mat Features Preserved Within the Siliciclastic Rock Record*, edited by J Schieber, PK Bose, PG Eriksson, S Banerjee, S Sarkar, W Altermann, and O Catuneanu, Elsevier Science, London, pp 5–38.

Gerdes G, Dunaftschik-Piewak K, Riege H, *et al.* (1994) Structural diversity of biogenic carbonate particles in microbial mats. *Sedimentology* 41:1273–1294.

Goltsman DSA, Denef VJ, Singer SW, *et al.* (2009) Community genomic and proteomic analyses of chemoautotrophic iron-oxidizing *Leptospirillum rubarum* (group II) and *Leptospirillum ferrodiazotrophum* (group III) bacteria in acid mine drainage biofilms. *Appl Environ Microbiol* 75:4599–4615.

Golubic S, Seong-Joo L, and Browne KM (2000) Cyanobacteria: architects of sedimentary structures. In *Microbial Sediments*, edited by RE Riding and SM Awramik, Springer-Verlag, Berlin, pp 57–67.

Gordon MW and Luna BL (1967) River flood plains: some observations on their formation. In *Geological Survey Professional Paper 282-C*, USA Government Printing Office, Washington, DC.

Grande JA, Borrego J, and Morales JA (1999) A study of heavy metal pollution in the Tinto-Odiel estuary in southwestern Spain using factor analysis. *Environ Geol* 39:1095–1101.

Grotzinger JP and Knoll AH (1999) Stromatolites in Precambrian carbonates: evolutionary mileposts or environmental dipsticks? *Annu Rev Earth Planet Sci* 27:313–358.

Hasiotis ST and Brake SS (2019) Macroscopic and microscopic morphological features of stromatolites related to activity of eukaryote-dominated biofilms in an acid mine drainage environment: biosignatures and understanding preservation of stromatolites as trace fossils. *Geomicrobiol J* 36:651–671.

Havig JR, Grettenberger C, and Hamilton TL (2017) Geochemistry and microbial community composition across a range of acid mine drainage impact and implications for the Neoarchean-Paleoproterozoic transition. *J Geophys Res Biogeosci* 122:1404–1422.

Hays LE, Graham HV, Des Marais DJ, *et al.* (2017) Biosignature preservation and detection in Mars analog environments. *Astrobiology* 17:365–400.

Hedrich S, Lünsdorf H, Kleeberg R, *et al.* (2011) Schwertmannite formation adjacent to bacterial cells in a mine water treatment plant and in pure cultures of *Ferrovum myxofaciens. Environ Sci Technol* 45:7685–7692.

Hofmann HJ, Grey K, Hickman AH, *et al.* (1999) Origin of 3.45 Ga coniform stromatolites in Warrawoona Group, Western Australia. *Geol Soc Am Bull* 111:1256–1262.

Huang LN, Kuang JL, and Shu WS (2016) Microbial ecology and evolution in the acid mine drainage model system. *Trends Microbiol* 24:581–593.

Ibarra Y and Corsetti F (2016) Lateral comparative investigation of stromatolites: astrobiological implications and assessment of scales of control. *Astrobiology* 16:271–281.

Ilbert M and Bonnefoy V (2013) Insight into the evolution of the iron oxidation pathways. *Biochim Biophys Acta* 1827:161–175.

Ishii T, Satoshi K, Nakagawa H, *et al.* (2015) From chemolithoautotrophs to electrolithoautotrophs: CO_2 fixation by Fe(II)-oxidizing bacteria coupled with direct uptake of electrons from solid electron sources. *Front Microbiol* 6:994.

Johnson DB (2014) Biomining—biotechnologies for extracting and recovering metals from ores and waste materials. *Curr Opin Biotechnol* 30:24–31.

Johnson DB and Aguilera A (2016) The microbiology of extremely acidic environments. In *Manual of Environmental Microbiology*, 4th ed., edited by M Yates, C Nakatsu, R Miller, and S Pillai, American Society for Microbiology Press, Washington, DC, pp. 4.3.1–24.

Johnson DB and Quatrini R (2016) Acidophile microbiology in space and time. In *Acidophiles: Life in Extremely Acidic Environments*, edited by R Quatrini and DB Johnson, Caister Academic Press, Poole, UK, pp 3–16.

Kalkowsky E (1908) Oolite and stromatolite in the North German red sandstone. *Zeitsch Deutsch Geolog Gesellsch* 60:68–125.

Kanellopoulos C, Thomas C, Xirokostas N, *et al.* (2019) Banded iron travertines at the Ilia hot spring (Greece): an interplay of biotic and abiotic factors leading to a modern Banded Iron Formation analogue? *Deposit Record* 5:109–130.

Kaplan HH, Ralph EM, Fernández-Remolar D, *et al.* (2016) Orbital evidence for clay and acidic sulfate assemblages on Mars based on mineralogical analogs from Rio Tinto, Spain. *Icarus* 275:45–64.

Kendall B, Reinhard CT, Lyons TW, *et al.* (2010) Pervasive oxygenation along late Archaean ocean margins. *Nat Geosci* 3:647–652.

Knoll AH (2003) The geological consequences of evolution. *Geobiology* 1:3–14.

Knoll AH, Carr M, Clark B, *et al.* (2005) An astrobiological perspective on Meridiani Planum. *Earth Planet Sci Lett* 240: 179–189.

Konhauser K (2007) *Introduction to Geomicrobiology*. Blackwell Science Ltd. & Blackwell Publishers, Oxford.

Konhauser KO, Lalonde SV, Planavsky NJ, *et al.* (2011) Aerobic bacterial pyrite oxidation and acid rock drainage during the Great Oxidation Event. *Nature* 478:369–373.

Korehi H, Blöthe M, Sitnikova MA, *et al.* (2013) Metal mobilization by iron- and sulfur-oxidizing bacteria in multiple extreme mine tailings in the Atacama Desert, Chile. *Environ Sci Technol* 47:2189–2196.

Kozubal MA, Macur RE, Zackary JJ, *et al.* (2012) Microbial iron cycling in acidic geothermal springs of yellowstone national park: integrating molecular surveys, geochemical processes, and isolation of novel Fe-active microorganisms. *Front Microbiol* 3:109.

Krumbein WE (1983) Stromatolites—the challenge of a term in space and time. *Precambrian Res* 20:493–531.

Lalonde SV and Konhauser KO (2015) Benthic perspective on Earth's oldest evidence for oxygenic photosynthesis. *Proc Natl Acad Sci U S A* 112:995–1000.

Leblanc M, Achard B, Ben Othman D, *et al.* (1996) Accumulation of arsenic from acidic mine waters by ferruginous bacterial accretions (stromatolites). *Appl Geochem* 11:541–554.

Logan BW, Hoffman P, and Gebelein CD (1974) Algal mats, cryptalgal fabrics, and structures, Hamelin Pool, Western Australia. In *Evolution and Diagenesis of Quaternary Carbonate Sequences, Shark Bay, Western Australia*, edited by BW Logan, JF Read, GM Hagan, P Hoffman, RG Brown, PJ Woods, and CD Gebelein, American Association of Petroleum Geologists, Tulsa, Oklahoma, Memoir 22, pp 140–194.

Loiselle L, McCraig MA, Dyar MD, *et al.* (2018) A spectral comparison of jarosites using techniques relevant to the robotic exploration of biosignatures on Mars. *Life (Basel)* 8:61.

López-Archilla AI and Amils R (1999) A comparative ecological study of two acidic rivers in southwestern Spain. *Microb Ecol* 38:146–156.

Lozano RP and Rossi C (2012) Exceptional preservation of Mn-oxidizing microbes in cave stromatolites (El Soplao, Spain). *Sed Geol* 255–256:42–55.

Luís AT, Novais MH, Van de Vijver B, *et al.* (2012) *Pinnularia aljustrelica* sp. nov. (Bacillariophyceae), a new diatom species found in acidic waters in the Aljustrel mining area (Portugal) and further observations on the taxonomy and ecology of *P. acidophila* Hofmann et Krammer and *P. acoricola* Hustedt. *Fottea* 12:27–40.

Luís AT, Durães N, Almeida SFP, *et al.* (2016) Integrating geochemical (surface waters, stream sediments) and biological (diatoms) approaches to assess AMD environmental impact in a pyritic mining area: aljustrel (Alentejo, Portugal). *J Environ Sci* 42:215–226.

Lukhele T, Selvarajan R, Nyoni H, *et al.* (2020) Acid mine drainage as habitats for distinct microbiomes: current knowledge in the era of molecular and omic technologies. *Curr Microbiol* 77:657–674.

Lundberg J and McFarlane DA (2011) Subaerial freshwater phosphatic stromatolites in Deer Cave, Sarawak. A unique geobiological cave formation. *Geomorphology* 128:57–72.

Macfarlane AJ, Docasal R, Rios C, *et al.* (2018) Improving accessibility and discovery of ESA planetary data through the new planetary science archive. *Planet Space Sci* 150:104–110.

Malarkey J, Baas JH, Hope JA, *et al.* (2015) The pervasive role of biological cohesion in bedform development. *Nat Commun* 6:6257.

Massocato TF (2018) Tolerance of *Ulothrix* sp. LAFIC 010 (Chlorophyta) against high concentration of metals from acid mine drainage. *Ecotoxicol Environ Safety* 157:227–234.

McKay CP (1992) Mars: a reassessment of its interest to biology. In *Space Exploration*, edited by GC Carle, DE Schwartz, and JL Huntington, Washington DC, NASA SP 512, pp 67–81.

McKay CP (2020) What is life—and when do we search for it on other worlds. *Astrobiology* 20:163–166.

Mesa V, Gallego JLR, González-Gil R, *et al.* (2017) Bacterial, archaeal, and eukaryotic diversity across distinct microhabitats in an Acid Mine Drainage. *Front Microbiol* 12;8:1756.

Mori JF, Lu S, Händel M, *et al.* (2017) Schwertmannite formation at cell junctions by a new filament-forming Fe(II)-oxidizing isolate affiliated with the novel genus *Acidithrix Microbiol* 162:62–71.

Nieto JM, Sarmiento AM, Olías M, *et al.* (2007) Acid mine drainage pollution in the Tinto and Odiel Rivers (Iberian Pyrite Belt, SW Spain) and bioavailability of the transported metals to the Huelva estuary. *Environ Int* 33:445–455.

Noffke N and Awramik S (2013) Stromatolites and MISS: differences between relatives. *GSA Today* 23:4–9.

Noffke N, Gerdes G, and Klenke T (2003) Benthic cyanobacteria and their influence on the sedimentary dynamics of peritidal depositional systems (siliciclastic, evaporitic salty and evaporitic carbonatic). *Earth Sci Rev* 12:1–14.

Noffke N, Beukes N, Bower D, *et al.* (2008) An actualistic perspective into Archean worlds -(cyano-)bacterially induced sedimentary structures in the siliciclastic Nhlazatse Section, 2.9 Ga Pongola Supergroup, South Africa. *Geobiology* 6:5–20.

Nordstrom, D and Southam, G. (1997). Geomicrobiology of sulfide mineral oxidation, in: geomicrobiology: Interactions between Microbes and Minerals. *Reviews in Mineralogy* 361–390.

Nordstrom DK, Blowes DW, and Ptacek CJ (2015) Hydrogeochemistry and microbiology of mine drainage: an update. *Appl Geochem* 57:3–16.

Oberholster PG, Genthe B, Hobbs P, *et al.* (2013) An ecotoxicological screening tool to prioritise acid mine drainage impacted streams for future restoration. *Environ Pollut* 176:244–253.

Packroff G and Woelfl S (2000) A review on the occurrence and taxonomy of heterotrophic protists in extreme acidic environments of pH values 3. *Hydrobiologia* 433:153–156.

Parenteau MN and Cady SL (2010) Microbial biosignatures in iron-mineralized phototrophic mats at Chocolate pots hot springs, Yellowstone National Park, United States. *Palaios* 25:97–111.

Phoenix VR, Bennett PC, Engel AS, *et al.* (2006) Chilean high-altitude hot-spring sinters: a model system for UV screening mechanisms by early Precambrian cyanobacteria. *Geobiology* 4:15–28.

Pilchin AN and Eppelbaum LV (2009) Iron and its unique role in Earth evolution. In *Monografías del Instituto de Geofísica* 9, UNAM, Mexico.

Planavsky N, Rouxel O, Bekker A, *et al.* (2009) Iron-oxidizing microbial ecosystems thrived in late Paleoproterozoic. *Earth Planet Sci Lett* 286:230–242.

Porada H and Bouougri EH (2007) Wrinkle structures: a critical review. *Earth Sci Rev* 81:199–215.

Poulton SW and Canfield DE (2011) Ferruginous conditions: a dominant feature of the ocean through Earth's history. *Elements* 7:107–112.

Preston LJ, Barcenilla R, Dartnell LR, *et al.* (2020) Infrared spectroscopic detection of biosignatures at Lake Tírez, Spain: implications for Mars. *Astrobiology* 20:15–25.

Rawlings DE and Johnson BD (2009) Ecology and biodiversity of extremophiles acidophiles microorganisms. In *Encyclopedia of Life Support Systems (EOLSS)*, Extremophiles Vol. III, edited by C Gerday and N Glansdorff, EOLSS Publishers, Oxford, pp 89–118.

Rickard D and Luther GW (2007) Chemistry of iron sulfides. *Chem Rev* 107:514–562.

Riding R (1999) The term stromatolite: towards an essential definition. *Lethaia* 32:321–330.

Riding RE (2011) Microbialites, stromatolites and thrombolites. In *Encyclopedia of Geobiology*, edited by J Reitner and V Thiel, Earth Science Series, Springer, Heidelberg, pp 635–654.

Rivera MJ, Luís AT, Grande JA, *et al.* (2019) Physico-chemical influence of surface water contaminated by acid mine drainage on the populations of diatoms in dams (Iberian Pyrite Belt, SW Spain). *Int J Environ Res Public Health* 16:4516.

Rohwerder T, Gehrke T, Kinzler K, *et al.* (2003) Bioleaching review part A. *Appl Microbiol Biotech* 63:239–248.

Sáez R, Pascual E, Toscano M, *et al.* (1999) The Iberian type of volcano–sedimentary massive sulphide deposits. *Mineral Deposit* 34:549–570.

Sallstedt T, Bengtson S, Broman C, *et al.* (2018) Evidence of oxygenic phototrophy in ancient phosphatic stromatolites from the Paleoproterozoic Vindhyan and Aravalli Supergroups, India. *Geobiology* 16:139–159.

Sánchez-España FJ, López Pamo E, Santofimia E, *et al.* (2005a) Acid mine drainage in the Iberian Pyrite Belt (Odiel river watershed, Huelva, SW Spain): geochemistry, mineralogy and environmental implications. *Appl Geochem* 20:1320–1356.

Sánchez-España FJ, López Pamo E, Santofimia E, *et al.* (2005b) The Tintillo acidic river (Rio Tinto mines, Huelva, Spain): an example of extreme environmental impact of pyritic mine wastes on the environment or an exceptional site to study acid-sulphate mine drainage systems? In *Proceedings Volume of the Securing the Future International Conference on Mining, Metals and the Environment*, Vol. I, Skellefteä, Sweden, pp 278–287.

Sánchez-España FJ, López-Pamo E, Santofimia E, *et al.* (2005c) The natural attenuation of two acidic effluents in Tharsis and La Zarza-Perrunal mines (Iberian Pyrite Belt, Spain). *Environ Geol* 49:253–266.

Sánchez-España FJ, López-Pamo E, Santofimia E, *et al.* (2006) The removal of dissolved metals by hydroxysulfate precipitates during oxidation and neutralization of acid mine waters, Iberian Pyrite Belt. *Aquat Geochem* 12:269–298.

Sánchez-España FJ, Santofimia E, and López Pamo E (2007) Iron terraces in acid mine drainage systems: a discussion about the organic and inorganic factors involved in their formation through observations from the Tintillo acidic river (Riotinto mine, Huelva, Spain). *Geosphere* 3:133–151.

Sánchez-España FJ, González Toril E, López Pamo E, *et al.* (2008) Biogeochemistry of a hyperacidic and ultra-concentrated pyrite leachate in San Telmo mine (Iberian Pyrite Belt, Spain). *Water Air Soil Pollut* 194:243–257.

Sánchez-España FJ, Yusta I, and Diez Ercilla M (2011) Schwertmannite and hydrobasaluminite: a re-evaluation of their solubility and control on the iron and aluminum concentration in acidic pit lakes. *Appl Geochem* 26:1752–1774.

Santa-Bárbara C and Valdés B (2008) Guide to the flora and vegetation of the Andévalo. *Faja pirítica España-Portugal, Consejería de Medio Ambiente.* Junta de Andalucía, España.

Sarmiento AM (2007) Study of the contamination by acid mine drainage of surface waters in the Odiel river basin (SW Spain). PhD Dissertation, Universidad de Huelva, Huelva, Spain.

Sarmiento AM, Nieto JM, Olías M, *et al.* (2008) Hydrochemical characteristics and seasonal influence on the pollution by acid mine drainage in the Odiel river basin (SW Spain). *Appl Geochem* 24:697–714.

Sarmiento AM, Grande JA, Luís AT, *et al.* (2018) Negative pH values in an open-air radical environment affected by acid mine drainage. Characterization and proposal of a hydrogeochemical model. *Sci Total Environ* 644:1244–1253.

Schippers A, Breuker A, Blazejak A, *et al.* (2010) The biogeochemistry and microbiology of sulfidic mine waste and bioleaching dumps and heaps, and novel Fe(II)-oxidizing bacteria. *Hydrometallurgy* 104:342–350.

Sevink J, Verstraten JM, Kooijman AM, *et al.* (2015) Rare moss-built microterraces in a high-altitude, Acid mine drainage polluted stream (Cordillera Negra, Peru). *Water Air Soil Pollut* 226:200–220.

Sheng Y, Bibby K, Grettenberger C, *et al.* (2016) Geochemical and temporal influences on the enrichment of acidophilic iron-oxidizing bacterial communities. *Appl Environ Microbiol* 82:3611–3621.

Sheng Y, Kaley B, Bibby K, *et al.* (2017) Bioreactors for low-pH iron(ii) oxidation remove considerable amounts of total iron. *RSC Adv* 7:35962–35972.

Shuster J, Rea MA, Etschmann B, *et al.* (2018) Terraced iron formations: biogeochemical processes contributing to microbial biomineralization and microfossil preservation. *Geosciences* 8:480–500.

Shuster J, Reith F, Izawa MRM, *et al.* (2017) Biogeochemical cycling of silver in acidic weathering environments. *Minerals* 7:218.

Spitzer J, Pielak GJ, and Poolman B (2015) Emergence of life: physical chemistry changes the paradigm. *Biol Direct* 10:33.

Tavira MR (2016) Hydrochemical characterization of the first AMD lixiviate that intercepts and contaminates the waters of the Odiel River as it passes through Mina Concepción. MSc thesis, Universidad Internacional de Andalucía, Huelva.

Verb RG, Morgan L, and Vis ML (2001) Macroalgal communities from an acid mine drainage impacted watershed. *Aquat Bot* 71:93–107.

Westall F (2005) Life on the early earth: a sedimentary view. *Science* 308:366–367.

Westall F, Loizeau D, Foucher F, *et al.* (2013) Habitability on Mars from a microbial point of view. *Astrobiology* 13:887–897.

Westall F, Foucher F, Bost N, *et al.* (2015) Biosignatures on Mars: what, Where, and How? Implications for the search for martian life. *Astrobiology* 15:998–1029.

Wielinga B, Lucy J, Moore J, *et al.* (1999) Microbiological and geochemical characterization of fluvially deposited sulfidic mine tailings. *Appl Environ Microbiol* 65:1548–1555.

Williams AJ, Alpers CN, Sumner DY, *et al.* (2017) Filamentous hydrous ferric oxide biosignatures in a pipeline carrying AMD at Iron Mountain Mine California. *Geomicrobiol J* 34: 193–206.

Address correspondence to:
Elizabeth Chacon-Baca
Facultad de Ciencias de la Tierra
Universidad Autónoma de Nuevo Léon (UANL)
Departamento de Geología
Carretera Cierro Prieto Km 8
Linares, Nuevo León
México 67700
México

E-mail: conophyton@gmail.com

Submitted 28 August 2019
Accepted 9 November 2020

Abbreviations Used

3D = three-dimensional
AMD = acid mine drainage
BIFs = banded iron formations
EC = electrical conductivity
EPS = extracellular polymeric substances
GOE = Global Oxygenation Event
IPB = Iberian Pyrite Belt
MISS = microbially induced sedimentary structures
SEM = scanning electron microscope
TIFs = terraced iron formations